


# Dominant Nonradiative Recombination Paths and Their Activation Processes in $\text{Al}_x\text{Ga}_{1-x}\text{N}$ -related Materials

Shuhei Ichikawa,<sup>‡</sup> Mitsuru Funato,<sup>\*</sup> and Yoichi Kawakami<sup>†</sup>

*Department of Electronic Science and Engineering, Kyoto University, Kyoto 615-8510, Japan*

 (Received 9 April 2018; revised manuscript received 4 September 2018; published 11 December 2018)

Dominant recombination paths in AlN and  $\text{Al}_x\text{Ga}_{1-x}\text{N}$ -related structures are investigated using cathodoluminescence (CL) mapping measurements and photoluminescence (PL) spectroscopy. The dark spot contrasts originating from nonradiative recombination at threading dislocations (TDs), which are observed in CL intensity maps, drastically decrease upon elevating the temperature. This is because carriers can reach TDs at low temperatures (9–60 K), but are captured by point defects (PDs) even in the vicinity of TDs near RT. Calculations based on the experimental results indicate that in the current AlN and Al-rich  $\text{Al}_x\text{Ga}_{1-x}\text{N}$  crystals, TDs scarcely affect the internal quantum efficiency (IQE) at RT as long as the TD density is less than  $2.6 \times 10^{10} \text{ cm}^{-2}$ . Because a TD density less than  $2.6 \times 10^{10} \text{ cm}^{-2}$  has already been achieved even for heteroepitaxially grown AlN films on sapphire substrates, it is evident that the most effective method to further improve the IQE of  $\text{Al}_x\text{Ga}_{1-x}\text{N}$ -related materials is to reduce PDs not TDs. Moreover, we clarify the existence of two types of PD states, which mainly degrade the emission efficiency, using temperature-dependent PL measurements. Combining the CL and PL results allows the activation energies of these PDs and TDs to be evaluated. Furthermore, we highlight the probability that PDs, which predominantly act as nonradiative recombination centers at room temperature, are complexes formed by Al vacancies and oxygen impurities that enhance the deep-level emissions at 3.2 and 3.5–3.7 eV near room temperature. Such a large impact of PDs on the efficiency degradation may be attributed to the high density of Al-vacancy-related PDs in AlN and Al-rich  $\text{Al}_x\text{Ga}_{1-x}\text{N}$  compared with that of Ga-vacancy-related PDs in GaN due to the small formation energy.

DOI: [10.1103/PhysRevApplied.10.064027](https://doi.org/10.1103/PhysRevApplied.10.064027)

## I. INTRODUCTION

Recently, group III nitride semiconductors have attracted attention for optical and electronic applications. Highly efficient InGaN-based light emitting diodes (LEDs) have been achieved in the blue spectral region [1]. Currently, laser diodes and LEDs emitting at other wavelengths are under development. For instance, AlN and  $\text{Al}_x\text{Ga}_{1-x}\text{N}$  with large energy band gaps (3.4–6.0 eV) are promising materials for harmless, high-efficiency deep ultraviolet (DUV) light-emitting devices, and they have potential in various applications such as air- or water-purification, high-density data storage, and biomedical research.

In principle,  $\text{Al}_x\text{Ga}_{1-x}\text{N}$  quantum wells (QWs) should exhibit a high internal quantum efficiency (IQE) because  $\text{Al}_x\text{Ga}_{1-x}\text{N}$  is a direct transition semiconductor and its radiative carrier recombination lifetime is short. Despite extensive studies on  $\text{Al}_x\text{Ga}_{1-x}\text{N}$ -based LEDs [2–6], the

external quantum efficiency (EQE) is low ( $< \sim 20\%$ ) in practice [7] compared with InGaN-based blue LEDs ( $> 80\%$ ) [1]. One of the reasons for the low EQE is related to the valence-band ordering in  $\text{Al}_x\text{Ga}_{1-x}\text{N}$ . Because the crystal-field splitting band is the topmost valence band in Al-rich  $\text{Al}_x\text{Ga}_{1-x}\text{N}$ , light extraction along the [0001] direction, which is a typical optical configuration of LEDs, becomes difficult at shorter wavelengths [8]. Moreover, we have reported that the IQE of  $\text{Al}_x\text{Ga}_{1-x}\text{N}$  QWs is remarkably degraded, especially under weak excitation conditions [9] and in the short-wavelength regions (Al-rich conditions) [10,11]. These observations are attributed to the many lattice defects in current  $\text{Al}_x\text{Ga}_{1-x}\text{N}$  crystals, which generate mid-gap levels (deep levels) that act as nonradiative recombination centers. Furthermore, lattice defects may also degrade the carrier injection efficiency (CIE) due to the enhanced carrier recombination in barrier layers. Although deep levels dominate the performances of  $\text{Al}_x\text{Ga}_{1-x}\text{N}$ -based devices, details about the nature (e.g., activation energies, capture cross sections, and trap densities) have yet to be comprehensively understood. For example, which types of defects predominantly degrade the efficiency has yet to be clarified.

<sup>\*</sup>funato@kuee.kyoto-u.ac.jp

<sup>†</sup>kawakami@kuee.kyoto-u.ac.jp

<sup>‡</sup>Present address: Division of Materials and Manufacturing Science, Osaka University, Osaka 565-0871, Japan

Many efforts have been made to reduce threading dislocations (TDs) as representative lattice defects [12–15]. High quality homoepitaxial films or QWs have recently been grown on AlN bulk substrates with a low threading dislocation density ( $TDD < 10^5 \text{ cm}^{-2}$ ) [16,17]. Even with a low TDD, the IQE under a weak excitation condition remains low ( $< 1\%$ ), and it is almost the same as that of QWs on sapphire substrates with a high TDD (approximately  $10^9\text{--}10^{10} \text{ cm}^{-2}$ ) [17]. This suggests that TDs may not act as the dominant nonradiative recombination centers. In fact, Chichibu *et al.* have suggested that point defects (PDs) impact the efficiency in AlN [18,19].

In this paper, we investigate the correlations of nonradiative recombination lifetimes and the activation energies of various lattice defects in  $\text{Al}_x\text{Ga}_{1-x}\text{N}$ -related materials using cathodoluminescence (CL) mapping measurements and photoluminescence (PL) spectroscopy. The CL intensity maps show dark-spot contrasts due to TDs at 9–60 K, but the contrasts disappear near RT, indicating dominant nonradiative recombination paths vary by temperature. To clarify the cause of the CL-contrast variation, the temperature dependence of the PL intensity is analyzed assuming the Arrhenius-type activation of nonradiative recombination processes. The activation energies derived from PL allow the CL-contrast variation due to temperature to be well reproduced. Thus, we identify the dominant nonradiative recombination paths (i.e., lifetime-killing defects) at each temperature, and propose a route to improve the IQE in AlN and Al-rich  $\text{Al}_x\text{Ga}_{1-x}\text{N}$  structures.

## II. EXPERIMENTAL PROCEDURES

AlN epitaxial films and Al-rich  $\text{Al}_x\text{Ga}_{1-x}\text{N}$ /AlN QWs are grown on AlN bulk substrates using the metalorganic vapor phase epitaxy (MOVPE) method. The substrates are prepared by the physical vapor transport method with (0001) (*c*-plane) or semipolar (1 $\bar{1}$ 02) (*r*-plane) surfaces. Both the *c*- and *r*-planes surfaces used in this paper are obtained by slicing bulk AlN ingots grown along the *r*-direction at different angles. Thus, their crystalline qualities are nominally identical, and TDD of the substrate observed by plan-view TEM is about  $5 \times 10^7\text{--}1 \times 10^8 \text{ cm}^{-2}$ . The surface treatments of the substrates prior to the epitaxy and detailed growth conditions are described elsewhere [17]. One remarkable difference between the *c*- and *r*-planes growths is the optimized reactor pressure, which is higher for *r*-plane growth (500 Torr) than for *c*-plane growth (76 Torr). The thickness of the *c*-plane (*r*-plane) AlN epitaxial film is about 1  $\mu\text{m}$  (400 nm). The well and barrier layer thicknesses of the fabricated  $\text{Al}_{0.8}\text{Ga}_{0.2}\text{N}$ /AlN 3QWs are about 1.5 and 15 nm, respectively. AlN homoepitaxial films and the QWs have very high structural qualities with atomically smooth surfaces and abrupt interfaces [17].

Temperature-dependent CL mapping is performed to characterize the carrier recombination processes in the AlN films and  $\text{Al}_{0.8}\text{Ga}_{0.2}\text{N}$ /AlN QWs in the temperature range between 9 and 293 K. CL intensity maps are taken under the panchromatic mode. The acceleration voltage of an electron beam for SEM and CL measurements is 5 kV. Thus, the CL signals are only from the epilayers. To precisely estimate the emission intensity without the influences of carbon deposition and charge-up due to the electron beam irradiation, temperature-dependent PL measurements are also performed for the AlN films. The excitation light source is a pulsed ArF excimer laser (193 nm) with a repetition frequency of 25 Hz and a pulse duration of 4 ns. The time-averaged excitation power density ranges from 110 to 910  $\text{kW}/\text{cm}^2$ . Because our samples are AlN films, the current laser condition can be regarded as a moderate excitation condition.

## III. RESULTS AND DISCUSSION

### A. Impact of TDs on efficiency degradation

#### 1. CL mapping

Because some of the excited carriers are captured by nonradiative recombination centers, the emission intensity reductions are often observed near extended defects such as TDs. This is the reason that extended defects are generally observed as dark spots or dark areas in CL (or PL) intensity maps. Figure 1(a) illustrates such a situation. Assuming isotropic carrier diffusion, the emission intensity  $I(r)$  in the vicinity of a TD is written as

$$I(r) = I_0 - I_D \exp\left(-\frac{r}{L_{\text{eff}}}\right), \quad (1)$$

where  $r$  is the distance from a TD,  $I_0$  is the emission intensity far from TDs,  $I_D$  is the intensity reduction just at TDs, and  $L_{\text{eff}}$  is the carrier diffusion length. (All the variables used in this paper are summarized in the Supplemental Material [20].)

It must be noted that Eq. (1) may underestimate the diffusion length unless a condition  $r \gg L_{\text{eff}}$  is satisfied [21,22]. However, extracting the precise diffusion length requires knowledge of the typical dimension of TDs and the recombination lengths at the surface and TD [22], which are currently unknown for  $\text{Al}_x\text{Ga}_{1-x}\text{N}$ . Therefore, we use the simplified equation. We consider that this approach hardly affects our analyses below, because what we discuss is not the *true* diffusion length, but the CL contrast, which is well reproduced with Eq. (1). Furthermore, the general relationship of (diffusion length) $^2 \propto$  (recombination lifetime) is used in the following discussion using  $L_{\text{eff}}$  in Eq. (1) instead of the true diffusion length, which also seems reasonable because the longer the true diffusion length, the longer the estimated  $L_{\text{eff}}$ . The validity of these arguments is discussed below.

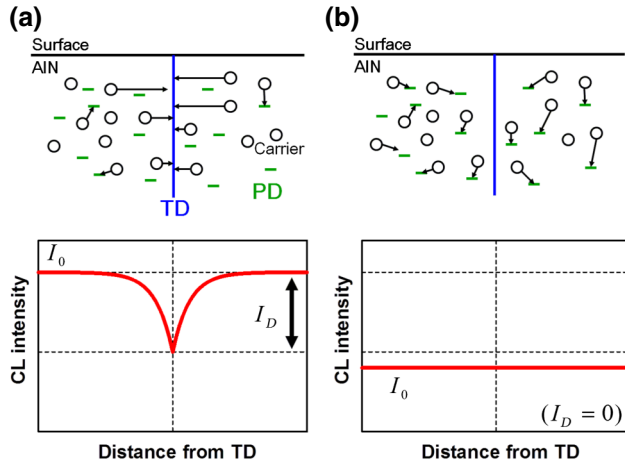


FIG. 1. Schematic images of the carrier recombination processes and the resultant variation of the emission intensity near TD when the dominant recombination centers are (a) TDs and (b) PDs.

Then the contrast of a dark spot due to a TD can be defined as

$$C_{\max} = \frac{I_D}{I_0}. \quad (2)$$

On the other hand, when PDs are the predominant non-radiative centers, dark spots cannot be observed near TDs. This is because, as shown in Fig. 1(b), most excited carriers are captured by PDs, which are assumed to be uniformly formed in the crystal, before reaching TDs. Note that dark spots hardly appear even when radiative recombination is the predominant process because most excited carriers radiatively recombine before reaching TDs in such a case. These considerations reveal that the impact of TDs strongly depends on the other recombination paths. A detailed characterization of the dark spots using CL mapping measurements is very useful to identify the dominant recombination path. Figure 2 shows the CL intensity maps of each sample and the SEM image of the *r*-plane AlN at 60 K (at the same place as the CL image of the *r*-plane AlN at 60 K). All CL mapping measurements are performed at structurally featureless areas. Figure 2(a) shows an example. The CL maps clearly show dark spots at low temperatures for the *c*- and *r*-planes AlN films, but the dark spot contrasts are drastically weakened at RT. Because the densities of the dark spots are comparable to TDDs in AlN substrates confirmed by plan-view TEM, the dark spots are attributed to TDs. On the other hand, dark spots are not observed in the CL images of *r*-plane  $\text{Al}_{0.8}\text{Ga}_{0.2}\text{N}/\text{AlN}$  QWs in the entire temperature region. The same tendency also occurs in *c*-plane Al-rich  $\text{Al}_x\text{Ga}_{1-x}\text{N}$  QWs. These results indicate that the dominant recombination paths depend on the temperature and sample structure.

To elucidate the carrier recombination processes in  $\text{Al}_x\text{Ga}_{1-x}\text{N}$ -related structures, the contrast variations in

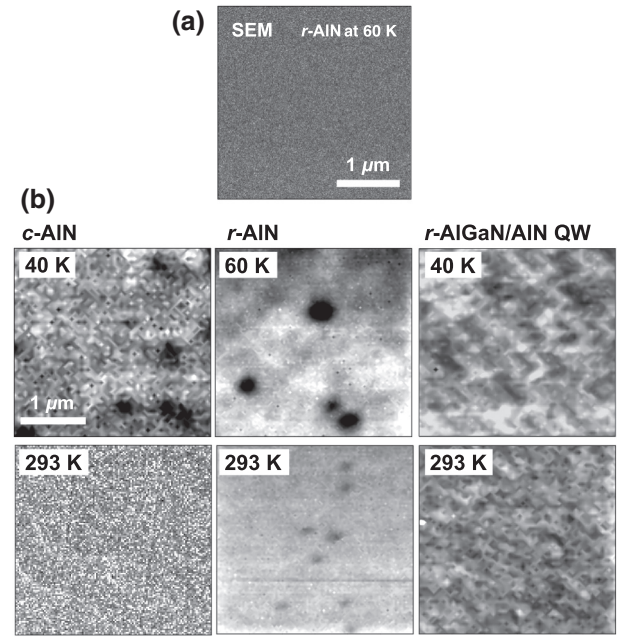


FIG. 2. (a) SEM image of the *r*-plane AlN surface. (b) CL intensity maps of AlN films and an *r*-plane  $\text{Al}_{0.8}\text{Ga}_{0.2}\text{N}/\text{AlN}$  QW at low temperatures and RT. Measured area is  $3 \mu\text{m}^2$  for all images. For *r*-plane AlN, the SEM image and CL image at 60 K are acquired at the same position.

the vicinity of the dark spots of *r*-plane AlN are carefully analyzed as a function of temperature [Figs. 3(a) and 3(b)]. The line profiles of the CL intensity across TDs are well fitted with Eq. (1). Figure 3(b) shows a representative example of the analyses for the *r*-plane AlN film. The experimental profiles quantify the temperature dependences of the carrier diffusion length  $L_{\text{eff}}$  and the dark spot contrast  $C_{\max}$ , as shown in Figs. 4 and 5, respectively. The carrier diffusion lengths cannot be determined for *c*-plane AlN at high temperatures or for the QWs at any temperature because dark spots are not observed in the CL intensity maps. It should be noted that the free excitonic emission is the dominant PL component of our *c*-plane AlN at 10–300 K [23,24]. Therefore, the temperature variations of  $L_{\text{eff}}$  and  $C_{\max}$  are not due to variations of the emission origin.

## 2. Diffusion length, $L_{\text{eff}}$

Figure 4 plots the determined carrier diffusion length  $L_{\text{eff}}$  in the *c*- and *r*-planes AlN films as functions of temperature. The carrier diffusion lengths in the AlN epilayers have certain maximum values. The diffusion length  $L_{\text{eff}}$  can generally be written as

$$L_{\text{eff}} = \sqrt{D_{\text{diff}} \times \tau_{\text{eff}}} = \sqrt{\frac{\mu k_B T}{e} \times \tau_{\text{eff}}}, \quad (3)$$

where  $D_{\text{diff}}$  is the diffusion coefficient, which can be rewritten by Einstein's relation using the carrier mobility  $\mu$ ,

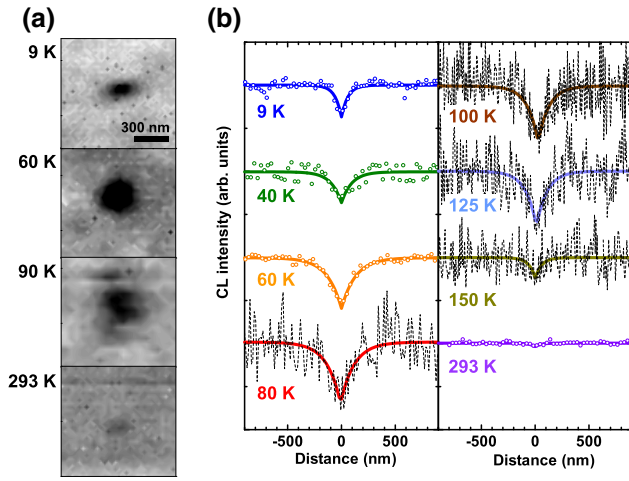


FIG. 3. (a) CL images showing the temperature dependence of the dark spot contrasts in the vicinity of TDs of *r*-plane AlN. (b) Symbols and dotted lines are the experimental CL intensity profiles across TDs in *r*-plane AlN at various temperatures. (Data plots are selected to clearly show the tendency of the contrast variation.) Solid lines show the results of the fits using Eq. (1). [Variation of SNRs (specifically between 60 and 80 K) is partially due to a difference in the exposure time for the CL mapping].

Boltzmann constant  $k_B$ , temperature  $T$ , and elementary electric charge  $e$ .  $\tau_{\text{eff}}$  is the effective carrier recombination lifetime.

For GaN, the role of TDs as recombination centers has been discussed experimentally [25–27] and theoretically [28]. However, the role of TDs is debatable for AlN. In this study, we assume that TDs affect the motion of excitons only in the vicinity of TDs, and the experimentally

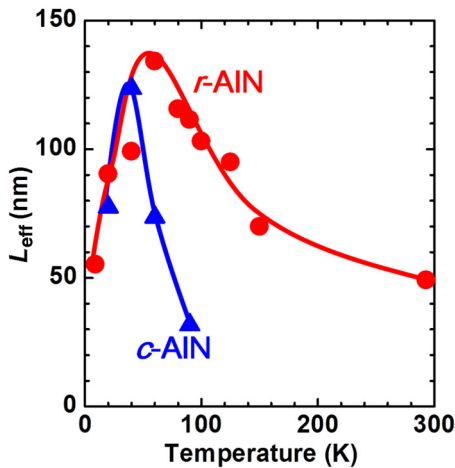


FIG. 4. Temperature dependences of the carrier diffusion lengths in the *c*- and *r*-planes AlN films. Solid curves are to guide the eyes.

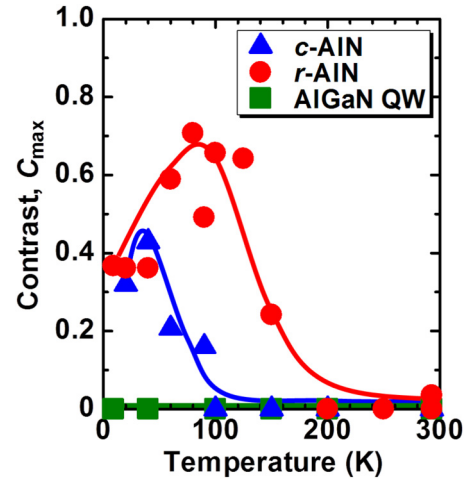


FIG. 5. Temperature dependences of the dark-spot contrasts in the AlN films and the *r*-plane  $\text{Al}_{0.8}\text{Ga}_{0.2}\text{N}/\text{AlN}$  QW. Solid curves are to guide the eyes.

acquirable diffusion length  $L_{\text{eff}}$  in Eqs. (1) and (3) is determined by the recombination rate in the areas far from TDs. These assumptions seem reasonable because the TDs in our samples are thoroughly isolated from each other and the typical carrier diffusion length of a few tens to hundreds of nm is much greater than the dislocation core size (approximately the length of the Burgers vector). Thus,  $\tau_{\text{eff}}$  is defined as

$$\frac{1}{\tau_{\text{eff}}} = \frac{1}{\tau_{\text{rad}}} + \frac{1}{\tau_p}, \quad (4)$$

where  $\tau_{\text{rad}}$  is the radiative recombination lifetime and  $\tau_p$  is the nonradiative recombination lifetime due to PDs.

Here, we describe the interpretation for the mobility and the carrier recombination lifetime of AlN and Al-rich  $\text{Al}_x\text{Ga}_{1-x}\text{N}$  used in this study. Electrons and holes in  $\text{Al}_x\text{Ga}_{1-x}\text{N}$ -related structures usually form pair states (excitons) even at RT due to the large exciton-binding energy. The diffusion coefficient of excitons may be limited by holes that are much heavier than electrons. In addition, nonradiative recombination lifetimes of excitons should be determined by the minority carriers because nonradiative recombination centers are occupied with majority carriers in many cases. We consider that the diffusion coefficients and the nonradiative recombination lifetimes in our undoped  $n^-$ -type  $\text{Al}_x\text{Ga}_{1-x}\text{N}$  samples are mainly determined by the holes' characteristics. It has been reported that the hole mobility in AlN is proportional to  $T^{-1.5}$  in the high temperature range  $> 300$  K due to phonon scattering [29]. Although no experimental and theoretical data are available for temperatures lower than 300 K, it is reasonable to assume that the hole mobility is proportional to  $T^m$  ( $m \geq -1.5$ ) at temperatures below RT, because other scattering mechanisms such as ionized impurity scattering ( $T^{1.5}$ ) may superimpose on phonon scattering. (Examples



for GaN can be found in Ref. [30].) For  $m = -1.5$ , which is the minimum value,  $\sqrt{D_{\text{diff}}} \propto T^{-0.25}$  is predicted from the Einstein's relation. Experimentally, on the other hand, because the temperature-induced decreases of  $L_{\text{eff}}$  in the  $r$ - and  $c$ -planes AlN films (Fig. 4) are well reproduced with  $T^{-0.65}$  and  $T^{-1.7}$ , respectively,  $L_{\text{eff}}$  is likely dominated not by  $\mu$  ( $D_{\text{diff}}$ ), but by  $\tau_{\text{eff}}$ . In other words,  $\tau_{\text{eff}}$  should decrease as the temperature increases. This finding along with Eqs. (3) and (4) indicate that  $\tau_p$  dominates the  $L_{\text{eff}}$  shortenings at higher temperatures because  $\tau_{\text{rad}}$  in the films is theoretically proportional to  $T^{+1.5}$ . The shorter  $L_{\text{eff}}$  in  $c$ -plane AlN indicates that the  $c$ -plane AlN film has more PDs (shorter  $\tau_p$ ) than the  $r$ -plane AlN film. The different PD densities may be due to the growth conditions, and a detailed explanation will be discussed elsewhere.

### 3. Dark-spot contrast $C_{\text{max}}$

Figure 5 shows the temperature dependences of the dark-spot contrasts in the AlN films and the  $r$ -plane  $\text{Al}_{0.8}\text{Ga}_{0.2}\text{N}/\text{AlN}$  QW. For the AlN films, dark spots are clearly observed at low temperatures (9–60 K), but their contrasts drastically decrease (or are eliminated) as the temperature increases (Fig. 3). Therefore, the temperature dependences of  $C_{\text{max}}$  also have maxima similar to  $L_{\text{eff}}$  (Fig. 5). This result indicates that the influence of PDs increases as the temperature increases. Hence, the recombination process in Fig. 1(b) becomes dominant over that in Fig. 1(a). On the other hand, dark spots are not observed in the CL image of the  $c$ - and  $r$ -planes  $\text{Al}_{0.8}\text{Ga}_{0.2}\text{N}/\text{AlN}$  QWs in the whole temperature region. The tendencies of the contrasts will be discussed in detail in Sec. III C, which suggest that the emission intensities from QWs are less affected by TDs than those of the AlN films.

### 4. Macroscopic impact of nonradiative recombination centers on efficiency degradation

The temperature dependences of  $L_{\text{eff}}$  and  $C_{\text{max}}$  enable us to estimate the efficiency degradation by TDs at various temperatures. The total intensity loss caused by one TD can be written as

$$\begin{aligned} i_{\text{Dtotal}} &= \int_0^\infty \int_0^{2\pi} \left[ I_D \exp\left(-\frac{r}{L}\right) \right] r d\theta dr \\ &= 2\pi L^2 I_D, \end{aligned} \quad (5)$$

where  $L$  is the carrier diffusion length considering the macroscopic impacts of TDs and PDs as described below. (When the dark spots are well isolated and TDs do not affect the carrier diffusion length,  $L = L_{\text{eff}}$ .)  $L$  is expressed by

$$L^2 = D_{\text{diff}} \times \tau_{\text{totalarea}}, \quad (6)$$

where  $\tau_{\text{totalarea}}$  is the macroscopic recombination lifetime determined by

$$\begin{aligned} \frac{1}{\tau_{\text{totalarea}}} &= \frac{1}{\tau_{\text{disarea}}} + \frac{1}{\tau_{\text{eff}}} \\ &= \frac{1}{\tau_{\text{disarea}}} + \frac{1}{\tau_{\text{rad}}} + \frac{1}{\tau_p}. \end{aligned} \quad (7)$$

Here,  $\tau_{\text{disarea}}$  means the macroscopically averaged nonradiative recombination lifetime due to TDs. (It should be noted that the variation in the carrier dynamics due to TDs is totally ascribed to the recombination lifetime, and the diffusion coefficient  $D_{\text{diff}}$  is assumed to be constant.) Moreover, the correlation between the IQE ( $\eta_{\text{IQE}}$ ) and  $\tau_{\text{totalarea}}$  is described by

$$\begin{aligned} \eta_{\text{IQE}} &= \frac{\tau_{\text{rad}}^{-1}}{\tau_{\text{disarea}}^{-1} + \tau_{\text{eff}}^{-1}} \\ &= \frac{\tau_{\text{totalarea}}}{\tau_{\text{rad}}}. \end{aligned} \quad (8)$$

Equations (6) and (8) lead to  $L^2 \propto \tau_{\text{totalarea}} \propto \eta_{\text{IQE}}$ .  $L^2$  can be rewritten as

$$L^2 = A \times \eta_{\text{IQE}}, \quad (9)$$

where  $A$  is a proportionality coefficient.

In areas sufficiently far from the dark spots due to TDs, the effective efficiency  $\eta_{\text{eff}}$  can be written as

$$\eta_{\text{eff}} = \frac{\tau_{\text{rad}}^{-1}}{\tau_{\text{rad}}^{-1} + \tau_p^{-1}} = \frac{\tau_{\text{eff}}}{\tau_{\text{rad}}}. \quad (10)$$

When TDs have a negligible impact on the macroscopic emission efficiency and carrier diffusion length,  $\eta_{\text{IQE}}$  and  $L$  are equal to  $\eta_{\text{eff}}$  and  $L_{\text{eff}}$ , respectively. Because Eq. (9) must be satisfied even in this situation,  $A$  can be written as  $L_{\text{eff}}^2/\eta_{\text{eff}}$ , and

$$L^2 = \frac{L_{\text{eff}}^2}{\eta_{\text{eff}}} \times \eta_{\text{IQE}}. \quad (11)$$

When  $I_{\text{max}}$  is defined as the emission intensity for 100% IQE,  $I_0$  and  $I_D$  are written as

$$I_0 = \eta_{\text{eff}} \times I_{\text{max}}, \quad (12)$$

and

$$\begin{aligned} I_D &= I_0 C_{\text{max}} \\ &= \eta_{\text{eff}} \times I_{\text{max}} C_{\text{max}}, \end{aligned} \quad (13)$$

respectively. Note that  $I_0$ ,  $I_D$ , and  $I_{\text{max}}$  are the emission intensities per unit area. Moreover, IQE can be described

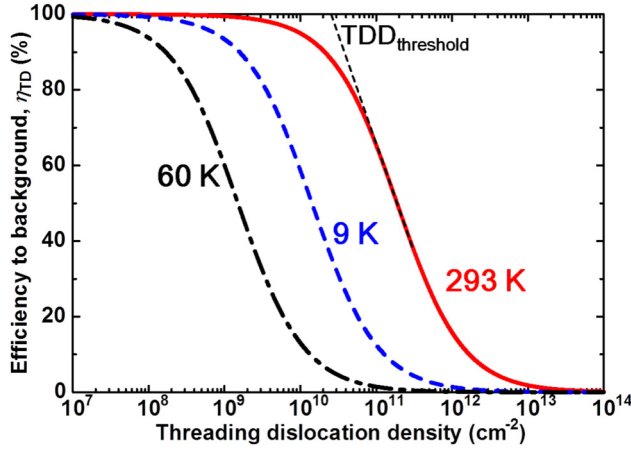


FIG. 6. Efficiency degradation due to TDs ( $\eta_{TD}$ ) in the  $r$ -plane AlN film. Broken, dash-dotted, and solid lines are the calculated results for 9, 60, and 293 K, respectively.

using Eqs. (5), (12), and (13) as

$$\eta_{IQE} = \frac{I_0 \times S - i_{Dtotal}(T_D \times S)}{I_{max} \times S} = \eta_{eff}(1 - 2\pi L^2 C_{max} T_D), \quad (14)$$

where  $T_D$  is TDD and  $S$  is the area of the measured region. Here,  $\eta_{IQE}$  is rewritten as

$$\eta_{IQE} = \eta_{eff} \times \eta_{TD}, \quad (15)$$

where  $\eta_{TD}$  is the efficiency with respect to  $\eta_{eff}$  and represents the impacts of TDs. ( $\eta_{TD} = 100\%$  means that the IQE is completely determined by PDs.) Then from Eqs. (11), (14), and (15),

$$\eta_{TD} = 1 - 2\pi L^2 C_{max} T_D = \frac{1}{1 + 2\pi L_{eff}^2 C_{max} T_D}. \quad (16)$$

[Equation (16) also relates  $L$  to  $L_{eff}$ , which is discussed in the Supplemental Material [20].]

Using the experimentally determined  $L_{eff}$  (Fig. 4) and  $C_{max}$  (Fig. 5), the  $\eta_{TD}$  values for the  $r$ -plane AlN film at certain temperatures are calculated as functions of TDD. Figure 6 shows the results. The impact of TDs strongly depends on the temperature.

To more quantitatively characterize the emission efficiency degradations due to TDs, we defined  $TDD_{threshold}$  as the extrapolation of  $\eta_{TD}$  to the 100% efficiency (Fig. 6), which corresponds to the lowest limit of TDD that degrades the emission efficiency. Figure 7 shows the estimated  $TDD_{threshold}$  for  $r$ - and  $c$ -planes AlN as functions of temperature. (In the Appendix, we indicate that the  $TDD_{threshold}$  values estimated using Eq. (1) and the recently

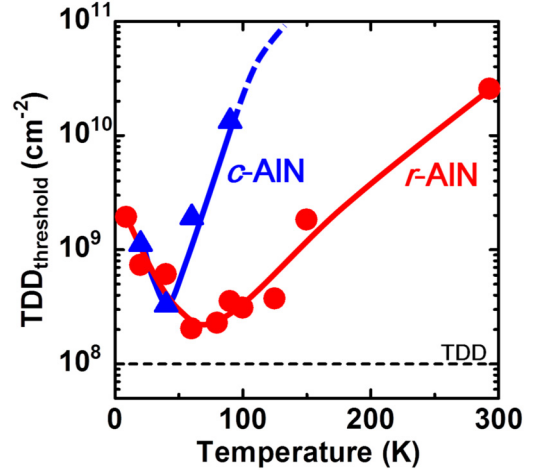


FIG. 7. Threshold TDDs defined as the lowest limits that degrade the IQE in the  $c$ - and  $r$ -planes AlN films.

proposed approach [22] are essentially the same, thereby confirming the validity of the present analysis procedure.) The IQE of the  $r$ -plane AlN film at RT is dominated by PDs when  $TDD < 2.6 \times 10^{10} \text{ cm}^{-2}$ . Because the  $c$ -plane AlN film has more PDs and  $\text{Al}_x\text{Ga}_{1-x}\text{N}/\text{AlN}$  QWs are less affected by TDs as described above,  $TDD_{threshold}$  is higher than that for the  $r$ -plane AlN film. Therefore, from a macroscopic viewpoint, TDs rarely act as major nonradiative recombination centers at RT as long as TDD is less than  $2.6 \times 10^{10} \text{ cm}^{-2}$ , regardless of whether AlN epitaxial films or  $\text{Al}_x\text{Ga}_{1-x}\text{N}$  QWs are heteroepitaxially grown. In fact, heteroepitaxial AlN films on sapphire substrates with  $TDD < 5 \times 10^9 \text{ cm}^{-2}$  have recently been reported [13,31,32]. Considering the reported TDDs of AlN films, the results in this study strongly suggest that the most effective method to improve the IQE in the current Al-rich  $\text{Al}_x\text{Ga}_{1-x}\text{N}$ -related structures is not to reduce TDs, but to reduce PDs.

It is noteworthy that the dark spots due to TDs are observed in the  $c$ - and  $r$ -planes AlN films at low temperatures, even though TDDs are less than  $TDD_{threshold}$  in the entire temperature range examined in this study (Fig. 7). This means that although TDs can act as nonradiative recombination centers, the influence is microscopically limited in the vicinity of TDs, and the macroscopic efficiency is predominantly determined by PDs over the entire temperature range.

As described above,  $TDD_{threshold}$  is an index of the impact of TDs on the efficiency degradation. However, it strongly depends on many factors such as temperature, PD density, sample structure, and alloy composition because these factors affect the carrier diffusion length  $L_{eff}$ . To simplify and generalize the discussion, the correlation between  $L_{eff}$  and  $TDD_{threshold}$  is calculated using Eq. (16). The effects due to the aforementioned factors are all included in  $L_{eff}$ . Figure 8 shows  $TDD_{threshold}$  as a function of  $L_{eff}$

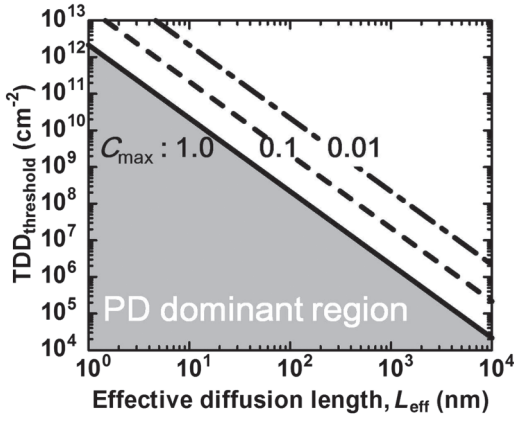


FIG. 8. Correlation between the carrier diffusion length and  $TDD_{\text{threshold}}$ . Solid line is the theoretical lowest limit of TDD, which affects the IQE regardless of the materials and structures.

using  $C_{\text{max}}$  as a parameter. Here, the larger the  $C_{\text{max}}$ , the greater the impact of TDs on the efficiency degradation [Eq. (16)], which leads to a lower  $TDD_{\text{threshold}}$ . The calculated  $TDD_{\text{threshold}}$  with  $C_{\text{max}} = 1.0$  indicates the theoretical lowest limit of TDD that will affect IQE regardless of the materials and structures. Therefore, PDs are the dominant nonradiative recombination centers in the shaded region of Fig. 8.

The reported hole diffusion lengths of GaN and Ga-rich  $\text{Al}_x\text{Ga}_{1-x}\text{N}$  films are several hundred nanometers [33–35]. They seem to be approaching the intrinsic material properties. If the hole diffusion lengths of undoped  $\text{Al}_x\text{Ga}_{1-x}\text{N}$ -related structures are also limited within approximately 1  $\mu\text{m}$  due to the intrinsic characteristics (radiative recombination processes), the reduction of TDDs less than  $10^6 \text{ cm}^{-2}$  does not improve the IQE regardless of the PD density.

It has often been reported that the TDD reduction from  $10^{10} \text{ cm}^{-2}$  to  $10^8 \text{ cm}^{-2}$  improves the emission efficiency of  $\text{Al}_x\text{Ga}_{1-x}\text{N}$  LEDs [3,36,37]. This finding appears inconsistent with our proposal. Although we have not reached a solid conclusion, this discrepancy has multiple plausible explanations. Generally, the TD movement requires the motion of intrinsic PDs such as vacancies and interstitials. Therefore, it is speculated that the growth conditions that reduce TDD can also reduce the PD density. Another possibility is impurity segregation to the TD core. As reported for GaN [38], intentional impurities such as Mg and unintentional impurities such as O can segregate around TDs. If a similar phenomenon occurs in AlN, TDD reduction may suppress the incorporation of impurities. Consequently, the emission efficiency increases because impurities often vary the Fermi level, strongly affecting the formation energy of intrinsic PDs and other impurity defects acting as non-radiative recombination centers. Particularly for AlN, the

growth temperature is higher than that for GaN, and elements from the substrate such as O from sapphire can easily diffuse into the AlN epitaxial film. In addition, the higher Al composition in our samples ( $\text{Al}_x\text{Ga}_{1-x}\text{N}$ ) than in typical LEDs may promote the formation of Al or Ga vacancies [39], which hide the role of TDs in determining the emission efficiency. Further studies are necessary to clarify the physics that determines the relationship between TDD and PD density.

## B. PL studies to determine the activation energies of PDs

### 1. Near-band-edge emission

Here, to clarify the correlation between the near-band-edge emission (NBE) intensity and the carrier recombination lifetimes, we consider the rate equation for excited carriers (excitons). The rate equation is generally expressed as

$$\frac{d\Delta p}{dt} = g - \frac{\Delta p}{\tau_{\text{total area}}}, \quad (17)$$

where  $\Delta p$  and  $g$  are the excess carrier density and the carrier generation rate, respectively. The left side of Eq. (17) is equal to zero under the equilibrium conditions. Thus,

$$\begin{aligned} \frac{\Delta p}{\tau_{\text{rad}}} &= \frac{\tau_{\text{total area}}}{\tau_{\text{rad}}} \times g \\ &= \eta_{\text{IQE}} \times g. \end{aligned} \quad (18)$$

Meanwhile, because  $\Delta p/\tau_{\text{rad}}$  is proportional to the NBE emission intensity  $I_{\text{NBE}}(T)$ , it is written as

$$I_{\text{NBE}}(T) = \eta_{\text{IQE}} \times I_{\text{max}} S. \quad (19)$$

where  $S$  is the measured area used in Eq. (14). When TDs are absent,  $\eta_{\text{IQE}}$  equals  $\eta_{\text{eff}}$ , and Eq. (12) is derived from Eq. (19).

In this study, we consider that nonradiative recombination centers trap carriers through multiphonon emissions (MPEs). In MPE processes, nonradiative recombination paths are explained by configuration coordinate diagrams [40], and the capture cross section of each defect is written as

$$\sigma_i(T) = \sigma_{0i} \exp\left(-\frac{E_{ai}}{k_B T}\right), \quad (20)$$

where  $\sigma_{0i}$  is the capture cross section at  $T \rightarrow \infty$  and  $E_{ai}$  is the activation energy, as shown in Fig. 9 ( $i$  is  $d$  or  $p$  for TDs or PDs, respectively). Then the nonradiative recombination lifetime due to each defect can be described

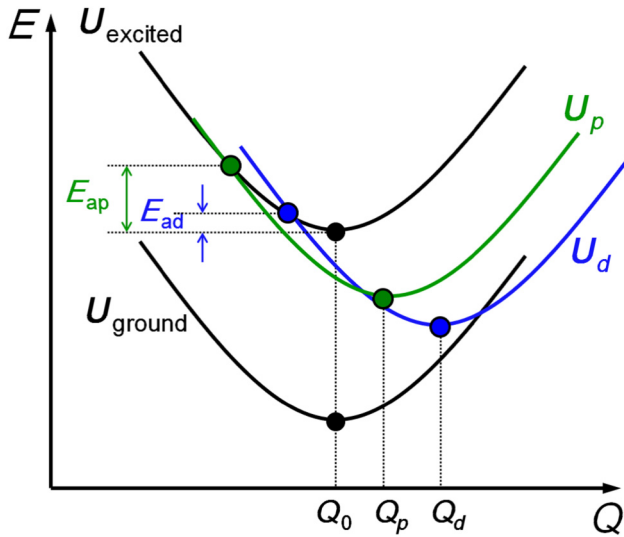


FIG. 9. Configuration coordinate diagram of the MPE process assuming TDs and PDs are different nonradiative recombination paths.

as

$$\begin{aligned}\tau_{\text{nonrad}} &= \frac{1}{v_{\text{th}} N_{\text{ti}} \sigma_i(T)} \\ &= \frac{1}{\sqrt{\frac{3k_B T}{m^*}} N_{\text{ti}} \sigma_{0i} \exp\left(-\frac{E_{\text{di}}}{k_B T}\right)},\end{aligned}\quad (21)$$

where  $m^*$  is the effective mass of carriers,  $v_{\text{th}}$  is the thermal velocity of carriers ( $=\sqrt{3k_B T/m^*}$ ), and  $N_{\text{ti}}$  is the trap volume density of each defect. Moreover, the radiative recombination lifetime is expressed by

$$\tau_{\text{rad}} = \alpha T^\gamma, \quad (22)$$

where  $\alpha$  and  $\gamma$  are constants that depend on the dimension of carrier confinement ( $\gamma = 3/2$  or  $1$  for bulk or ideal QW,

respectively) [41,42]. From Eqs. (12), (21), and (22), the temperature dependence of  $I_0$  can be written as

$$\begin{aligned}I_0(T) &= \eta_{\text{eff}} \times I_{\text{max}} \\ &= \frac{\tau_{\text{rad}}^{-1}}{\tau_{\text{rad}}^{-1} + \tau_p^{-1}} \times I_{\text{max}} \\ &= \frac{I_{\text{max}}}{1 + \alpha T^\gamma \sqrt{\frac{3k_B T}{m^*}} \sum_{s=1}^n N_{\text{tps}} \sigma_{0ps} \exp\left(-\frac{E_{\text{aps}}}{k_B T}\right)}.\end{aligned}\quad (23)$$

Here, to reproduce the experimental results shown below, multiple types of PDs are assumed (the number of the types is  $n$ ), and TDs are neglected due to the following reason. From a macroscopic point of view (Fig. 7), TDDs in our samples are sufficiently low and have a negligible effect on the emission efficiency degradation in the whole temperature region. Therefore, thermal quenching in our samples observed by the macroscopic measurements is ascribed to only PDs, and the emission intensity  $I_{\text{NBE}}(T) \approx I_0(T)S$ .

We perform macroscopic PL measurements for the  $r$ -plane AlN homoepitaxial film. Figure 10 shows the PL spectra at low temperature and RT. In addition to NBE emissions, deep-level emissions are observed. The peak intensity (and the integrated intensity) of the NBE emission is much stronger than those of the deep-level emissions regardless of temperature.

Figure 11 plots the temperature dependences of the integrated PL intensities of NBE emissions under various excitation powers. Under any excitation condition, two different types of thermal quenching are observed at 10–200 and 200–300 K. Two-step thermal quenching is also observed in the  $c$ -plane AlN film. These results indicate that two types of PDs with different activation energies  $E_{\text{ap}1}$  and  $E_{\text{ap}2}$  predominantly act as nonradiative recombination centers in Al-rich  $\text{Al}_x\text{Ga}_{1-x}\text{N}$ -related structures.

Assuming  $n = 2$  in Eq. (23),  $I_{\text{NBE}}(T)$  is expressed as

$$I_{\text{NBE}}(T) = \frac{I_{\text{max}} S}{1 + \alpha T^\gamma \sqrt{\frac{3k_B T}{m^*}} \left[ N_{\text{tp}1} \sigma_{0p1} \exp\left(-\frac{E_{\text{ap}1}}{k_B T}\right) + N_{\text{tp}2} \sigma_{0p2} \exp\left(-\frac{E_{\text{ap}2}}{k_B T}\right) \right]} \quad (24)$$

$$\approx \frac{I_{\text{max}} S}{1 + a \exp\left(-\frac{E_{\text{ap}1}}{k_B T}\right) + b \exp\left(-\frac{E_{\text{ap}2}}{k_B T}\right)}, \quad (25)$$

where  $a$  and  $b$  are approximated to be constants. Although Eq. (24) is stricter, Eq. (25) is often used to estimate the activation energy because the exponential term varies

more significantly than the  $T^{\gamma+1/2}$  term due to temperature. PDs that cause the first (at 10–200 K) and the second (at 200–300 K) thermal quenchings are referred to as P1 and P2, respectively. Thermal quenching due to those PDs is well fitted with Eq. (25), as shown by the solid lines in Fig. 11. The estimated activation energies of P1 and



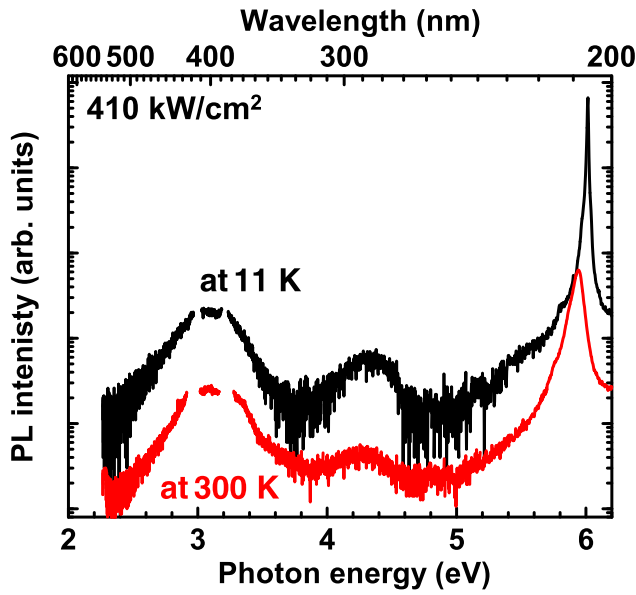


FIG. 10. PL spectra of the *r*-plane AlN film at 11 and 300 K. Two breaks at approximately 3.0 and 3.2 eV are due to masking of the second-order diffractions of the AlN band-edge emission and excitation laser, respectively.

P2 are  $E_{ap1} \sim 10$  and  $E_{ap2} \sim 130$  meV, regardless of the excitation power. However, stronger excitation conditions lead to weaker thermal quenching due to the occupation of P1 and P2 by photoexcited carriers [9]. Note that both of the estimated activation energies are considerably different from the exciton binding energy of AlN (53.7 meV) [43]. This result indicates that thermal quenching is mainly caused by the activation of PDs and not exciton dissociation.

## 2. Deep-level emissions

Figure 12 shows the variations in the deep-level emission spectra of the *r*-plane AlN film due to temperature. (To clearly see deep-level emissions, the second-order diffractions of the AlN band-edge emission and excitation laser are avoided by inserting a long-wavelength pass filter ( $> 250$  nm) between the sample and monochromator.) The deep-level emissions peaking at 3.0 and 4.3 eV are predominantly observed at low temperatures and become weaker as the temperature increases. The emission around 3.0 eV cannot be well separated, but the shoulders at approximately 3.3 and 3.8 eV suggest that various components are involved. On the other hand, the origin of the emission at 4.3 eV is often ascribed to defects related to carbon impurities [44]. However, it is uncertain whether this is the case in our samples because the carbon impurities in our samples are below the detection limit ( $< 2 \times 10^{16} \text{ cm}^{-3}$ ) of secondary ion mass spectrometry (SIMS). Unlike the aforementioned deep-level emissions at 3.0 and

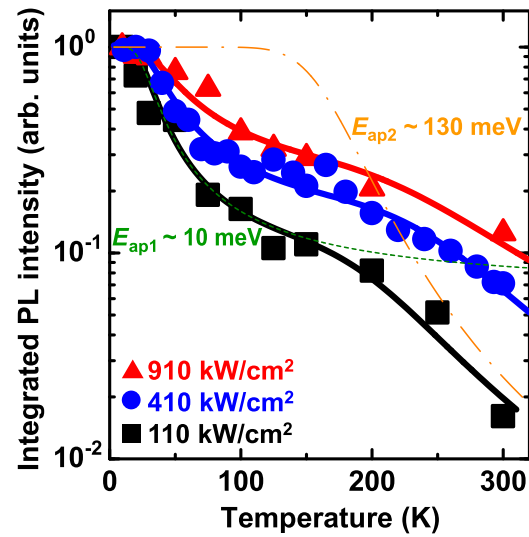


FIG. 11. Integrated PL intensities of NBE emission of the *r*-plane AlN film under various excitation powers. Intensities are normalized by the maximum intensity of each excitation condition. Solid lines are the results of the fits with Eq. (25) assuming two different PDs, P1 and P2.

4.3 eV, the emissions at approximately 3.2 and 3.5–3.7 eV are pronounced above 200 K. The emission enhancement means that the carrier transfer to the deep-level states is promoted as the temperature increases.

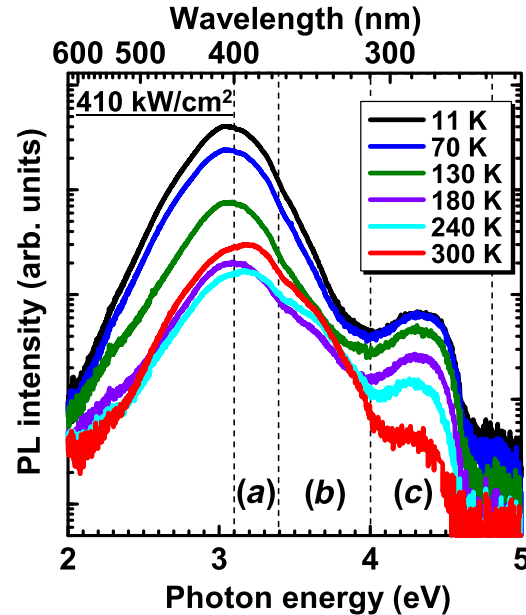


FIG. 12. Deep-level emission spectra of the *r*-plane AlN film at various temperatures. Spectral ranges (a), (b), and (c), which span 3.1–3.4, 3.4–4.0, and 4.0–4.8 eV, respectively, show distinct PL behaviors. Emission intensity enhancement is clearly observed for the emissions at approximately 3.2 and 3.5–3.7 eV above 200 K.

To further investigate the thermal quenching and a carrier transfer, we perform numerical analyses based on the rate equation. The rate equation for deep-level emissions can be expressed as

$$\frac{d\Delta p_D}{dt} = g_D - \frac{\Delta p_D}{\tau_{D\text{rad}}} - \frac{\Delta p_D}{\tau_{D\text{nonrad}}} + \frac{\Delta p}{\tau_{\text{trans}}}, \quad (26)$$

where  $\Delta p_D$  and  $g_D$  are the excess carrier (exciton) density in the deep-level state and the generation rate of carriers directly excited from the ground state to the deep-level state, respectively.  $\tau_{D\text{rad}}$  and  $\tau_{D\text{nonrad}}$  are the carrier recombination lifetimes for  $\Delta p_D$  with and without deep-level emissions, respectively. Note that  $\Delta p$  is the excess carrier density in the excited state (not in the deep-level state) and  $\tau_{\text{trans}}$  is the carrier transfer lifetime from the excited state to the deep-level state. Therefore, the last term of Eq. (26) represents the carrier transfer rate from the excited state. At equilibrium,  $d\Delta p_D/dt = 0$ . Thus,

$$\frac{\Delta p_D}{\tau_{D\text{rad}}} = \frac{\tau_{D\text{rad}}^{-1}}{\tau_{D\text{rad}}^{-1} + \tau_{D\text{nonrad}}^{-1}} \left( g_D + \frac{\Delta p}{\tau_{\text{trans}}} \right). \quad (27)$$

From Eqs. (18) and (19),  $\Delta p$  can be expressed as

$$\Delta p = \frac{I_{\text{NBE}}(T)}{I_{\text{max}}S} \times g \times \tau_{\text{rad}}. \quad (28)$$

Substituting Eq. (28) into Eq. (27) gives

$$\frac{\Delta p_D}{\tau_{D\text{rad}}} = \frac{g_D}{1 + \tau_{D\text{rad}}\tau_{D\text{nonrad}}^{-1}} \times \left( 1 + \frac{gI_{\text{NBE}}(T)}{gDI_{\text{max}}S} \times \frac{\tau_{\text{rad}}}{\tau_{\text{trans}}} \right). \quad (29)$$

$\Delta p_D/\tau_{D\text{rad}}$  is proportional to the deep-level emission intensity  $I_{\text{Deep}}$ .  $\tau_{\text{trans}}$  is one of the nonradiative recombination lifetimes for the carriers in the excited state. Therefore,  $\tau_{D\text{nonrad}}$  and  $\tau_{\text{trans}}$  can be expressed in the same form as Eq. (21). Applying the same approximation as in Eq. (25) yields

$$I_{\text{Deep}}(T) \approx \frac{1 + dI_{\text{NBE}}(T) \exp\left(-\frac{E_{a2}}{k_B T}\right)}{1 + c \exp\left(-\frac{E_{a1}}{k_B T}\right)} \times I_{\text{Deep}}(0), \quad (30)$$

where  $I_{\text{Deep}}(0)$  is the deep-level emission intensity at  $T = 0$  K.  $c$  and  $d$  are constants related to the thermal quenching and carrier transfer to the deep level, respectively.  $E_{a1}$  and  $E_{a2}$  are the respective activation energies. For simplicity, we assume a single recombination path for thermal quenching of the deep-level emission. To exactly consider the temperature dependence of  $\Delta p$ , the same excitation power should be used for  $I_{\text{NBE}}(T)$  and for  $I_{\text{Deep}}(T)$  in Eq. (30) because  $I_{\text{NBE}}(T)$  strongly depends on the excitation power (Fig. 11).

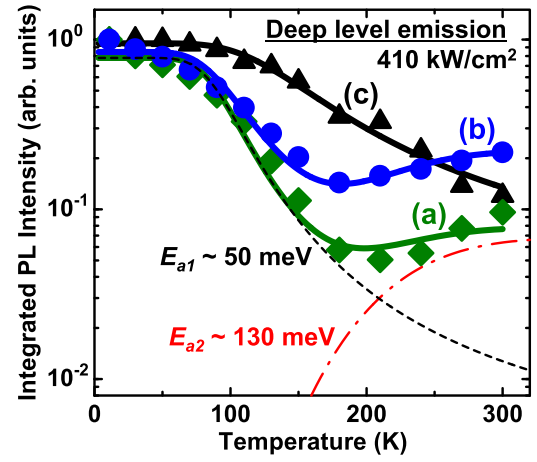


FIG. 13. Integrated PL intensities of deep-level emissions of the *r*-plane AlN film as functions of temperature. Emission intensities are integrated in ranges (a)–(c), defined in Fig. 12. Solid lines are the results of the fits with Eq. (30) assuming the activation energies  $E_{a1}$  and  $E_{a2}$  for the thermal quenching and the carrier transfer to the deep levels, respectively.

Although Eq. (30) assumes only a single deep-level state, the broad PL spectra shown in Fig. 12 apparently consist of multiple components, which are difficult to unambiguously separate by multicomponent spectral fit. Therefore, the PL intensities are integrated in three different spectral ranges [(a)–(c) in Fig. 12], which indicate distinctive behaviors. The spectral ranges, which span (a) 3.1–3.4 eV, (b) 3.4–4.0 eV, and (c) 4.0–4.8 eV, are used in the discussion with Eq. (30).

Figure 13 plots the temperature dependences of the integrated deep-level emission intensities in ranges (a)–(c) of the *r*-plane AlN film. The thermal behavior of the deep-level emission intensity integrated in the full spectral range (2.0–5.0 eV) is almost the same as that in range (a). In ranges (a) and (b), the emission intensities are thermally quenched below 200 K, but are enhanced above 200 K due to the emissions peaking at approximately 3.2 and 3.5–3.7 eV, respectively. In range (c), the integrated PL intensity is dominated by the emission at 4.3 eV. Thermal quenching is monotonic, which differs from ranges (a) and (b).

The solid lines in Fig. 13 are the fitted lines with Eq. (30). The fits agree well with the experimental results.  $I_{\text{NBE}}(T)$  under the same excitation conditions (410 kW/cm<sup>2</sup>) as Fig. 12 is used for the fits. The estimated activation energy of the thermal quenching ( $E_{a1}$ ) is approximately 50 meV for all spectral ranges, and that of the carrier transfer ( $E_{a2}$ ) is approximately 130 meV for ranges (a) and (b). It is noteworthy that  $d$  in range (c) is negligible and the emission intensity is not enhanced. This is probably because the trap density or the capture cross section of the deep-level state related to the 4.3-eV emission is too small to capture the excess carriers in the excited state.

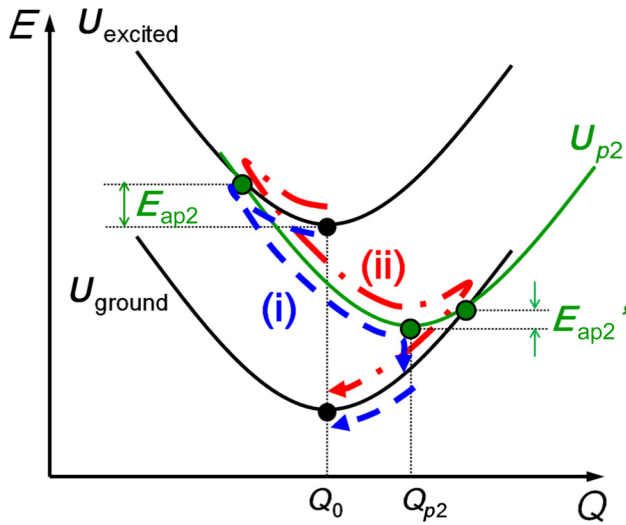


FIG. 14. Carrier transfer or recombination paths mediated by P2 in the configuration coordinate diagrams. Path (i) causes radiative deep-level emissions and path (ii) is completely non-radiative.

As a result, the majority of the carriers are transferred to other deep-level states at elevated temperatures, and only thermal quenching is observed in range (c).

The estimated  $E_{a1}$  differs from the activation energies of the aforementioned PDs ( $E_{ap1}$  and  $E_{ap2}$ ) because the thermal quenching of the deep-level emissions and that of the NBE emission are completely different phenomena. Figure 14 shows the configuration coordinate diagrams among the ground state ( $U_{\text{ground}}$ ), excited state ( $U_{\text{excited}}$ ), and deep-level state due to P2 ( $U_{p2}$ ).  $E_{ap2}$  is related to thermal quenching of the NBE emission, whereas  $E'_{ap2}$  is related to that of the deep-level emission. Therefore,  $E_{ap2}$  and  $E'_{ap2}$  differ in most cases. In addition, carrier transfer from  $U_{p2}$  to other deep-level states causes thermal quenching of the  $U_{p2}$ -related emission. Therefore, the estimated  $E_{a1}$  can differ from  $E_{ap1}$  and  $E_{ap2}$ .

The estimated  $E_{a1}$  ( $\sim 50$  meV) has almost the same value in the entire spectral ranges (a)–(c) despite the fact that it should be related to different deep-level states. Considering  $E_{a1}$  is very close to the exciton binding energy of AlN (53.7 meV) [43], the thermal quenching of the deep-level emissions in ranges (a)–(c) is ascribed to exciton dissociation, and  $E'_{ap2}$  in Fig. 14 is limited by the exciton binding energy.

Because the thermal quenching of the NBE emission above 200 K is dominated by P2, the deep-level emission enhancements above 200 K in ranges (a) and (b) (Fig. 13) may be related to P2 activation. When P2 is activated by elevating the temperature, holes in  $U_{\text{excited}}$  are trapped by P2 and transferred to  $U_{\text{ground}}$  through path (i) or path (ii) in Fig. 14. In the case of path (i), a deep-level emission

with an energy corresponding to the transition from the  $U_{p2}$  bottom to  $U_{\text{ground}}$  occurs. Consequently, the deep-level emission is enhanced. In fact, the activation energy of P2 ( $E_{ap2} \sim 130$  meV) is almost the same as the transfer activation energy  $E_{a2}$  ( $\sim 130$  meV), which suggests that P2 activation enhances the deep-level emission. Regardless of the enhanced carrier transfer to the P2 state at elevated temperatures, the total deep-level emission intensity is weaker than that at low temperatures. This is because recombination path (ii) is a completely nonradiative process without any deep-level emissions and the carriers captured by P2 recombine through either path (i) or (ii). It is noteworthy that the deep-level emission enhancement related to P1 activation ( $E_{ap1} \sim 10$  meV) is not observed, which suggests that P1 activation is not accompanied by deep-level emissions.

Because the enhanced emissions at 3.2 and 3.5–3.7 eV are due to the carrier transfer to P2, these emissions may provide crucial information about the origin of P2. Although various PDs in AlN lead to the deep-level emissions [44–47], impurities, which are a type of PD, may be excluded as a possible origin of P2 because undoped AlN homoepitaxial films have very low densities of impurities such as silicon, carbon, and oxygen (in some cases, below the detection limit of SIMS [23]). Moreover, the formation energies of various PDs in AlN have been calculated [39,48,49], and those of Al vacancies ( $V_{\text{Al}}$ ) and their complex defects in AlN with  $n$ -type conductivity are remarkably lower than those of simple substitutional impurity defects.  $V_{\text{Al}}$ -related defects are presumed to more easily form during the growth of undoped AlN or undoped Al-rich  $\text{Al}_x\text{Ga}_{1-x}\text{N}$ . The  $V_{\text{Al}}$ -related defects act as acceptorlike defects and are the most stable in fully negative-charged states when the Fermi level is in the upper part of the band gap. Especially, a  $V_{\text{Al}}\text{-O}_\text{N}$  complex defect is easily formed in  $n$ -type AlN ( $\text{O}_\text{N}$  is a substitutional oxygen impurity defect), and the formation energies of  $(V_{\text{Al}}\text{-O}_\text{N})^{2-}$  and  $(V_{\text{Al}}\text{-}2(\text{O}_\text{N}))^-$  are lower than that of  $V_{\text{Al}}$  for most Fermi level positions [49]. Such fully negative-charged states of  $V_{\text{Al}}\text{-O}_\text{N}$  complexes are unable to capture additional electrons. However, once such defects capture holes to become  $(V_{\text{Al}}\text{-O}_\text{N})^-$  and  $(V_{\text{Al}}\text{-}2(\text{O}_\text{N}))^0$  states, they can capture electrons with emissions at 3.2 and 3.5 eV, respectively [49]. After electron capture accompanied by the deep-level emissions, these states return to the fully negative-charged states again (Fig. 15). Because the deep-level emissions at 3.2 and 3.5–3.7 eV are enhanced by hole transfer to P2, the dominant nonradiative recombination center P2 may be a fully negative-charged  $V_{\text{Al}}\text{-O}_\text{N}$  complex defect. Although we cannot completely identify the origin of P2 as either  $(V_{\text{Al}}\text{-O}_\text{N})^{2-}$  or  $(V_{\text{Al}}\text{-}2(\text{O}_\text{N}))^-$ , we consider that P2 is likely to be a  $(V_{\text{Al}}\text{-}2(\text{O}_\text{N}))^-$  defect because the deep-level emission at 3.5–3.7 eV is more significantly enhanced than that at 3.2 eV (Fig. 13).

### C. Combined analyses of CL and PL

#### 1. Microscopic impacts of nonradiative recombination centers in the vicinity of TDs

Here, the temperature dependence of the dark-spot contrasts in the CL mapping is explained using the activation energies derived from the PL measurements and the difference between AlN and GaN is discussed. Although the impact of TDs is macroscopically negligible, its influence near TDs must be considered to explain the dark-spot

contrast. The nonradiative recombination lifetime in the close vicinity of TD is defined as  $\tau_D$ , which can be written as Eq. (21) (where  $i = d$ ). Here, it should be noted that  $N_{td}$  is not the areal density of TDs, but the volume density of traps due to TD. In other words,  $N_{td}$  is the volume trap density near the dislocation core and is equal to zero far from TDs. Therefore, the microscopic emission intensity in the vicinity of TD [ $r = 0$  in Eq. (1)] is determined by the lifetimes  $\tau_D$ ,  $\tau_p$ , and  $\tau_{rad}$ , which is given as

$$I_0(T) - I_D(T) = \frac{\tau_{rad}^{-1}}{\tau_{rad}^{-1} + \tau_d^{-1} + \tau_p^{-1}} \times I_{max} = \frac{I_{max}}{1 + \alpha T^\gamma \sqrt{\frac{3k_B T}{m^*}} \left[ N_{td} \sigma_{0d} \exp\left(-\frac{E_{ad}}{k_B T}\right) + N_{tp1} \sigma_{0p1} \exp\left(-\frac{E_{ap1}}{k_B T}\right) + N_{tp2} \sigma_{0p2} \exp\left(-\frac{E_{ap2}}{k_B T}\right) \right]}. \quad (31)$$

The CL contrast  $C_{max}$  can be written using Eqs. (2), (23) (where  $n = 2$ ), and (31) as

$$C_{max}(T) = \frac{I_D(T)}{I_0(T)} = \frac{\alpha T^\gamma \sqrt{\frac{3k_B T}{m^*}} N_{td} \sigma_{0d} \exp\left(-\frac{E_{ad}}{k_B T}\right)}{1 + \alpha T^\gamma \sqrt{\frac{3k_B T}{m^*}} \left[ N_{td} \sigma_{0d} \exp\left(-\frac{E_{ad}}{k_B T}\right) + N_{tp1} \sigma_{0p1} \exp\left(-\frac{E_{ap1}}{k_B T}\right) + N_{tp2} \sigma_{0p2} \exp\left(-\frac{E_{ap2}}{k_B T}\right) \right]}. \quad (32)$$

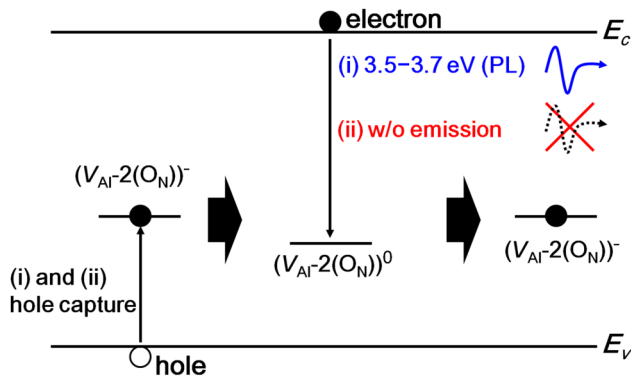


FIG. 15. Schematic image of hole capture mediated by the  $(V_{Al}-2(O_N))^-$  state and the following deep-level emission. (i) and (ii) are the carrier paths illustrated in Fig. 14.

The solid lines in Figs. 16(a) and 16(b) show the fitted temperature dependence of CL contrasts in the  $c$ - and  $r$ -planes

AlN films using Eq. (32). We used  $E_{ad}$  and  $F_i$  ( $i = d, p1$ , and  $p2$ ) as the fitting parameters, where  $F_i$  is defined as

$$F_i = \alpha \sqrt{\frac{3k_B}{m^*}} N_{ti} \sigma_{0i}. \quad (33)$$

Note that  $E_{ap1}$  ( $\sim 10$  meV) and  $E_{ap2}$  ( $\sim 130$  meV) in the fits are fixed based on estimates of the PL measurements in Sec. III B. Furthermore,  $E_{ad}$  and  $F_d$  are common to the  $c$ - and  $r$ -planes AlN films because both substrates are sliced from similarly grown AlN ingots and  $\tau_D$  (as well as  $E_{ap1}$  and  $E_{ap2}$ ) should be intrinsically determined by the material. Assuming  $\gamma = 3/2$  for the AlN films, the fitting curves are uniquely determined. The estimated activation energy of TDs ( $E_{ad}$ ) is approximately 2.5 meV from these fits. Table I shows the activation energies of the dominant nonradiative recombination centers near TDs.

Figures 16(d) and 16(e) show the correlations of radiative and nonradiative recombination lifetimes in the  $c$ - and



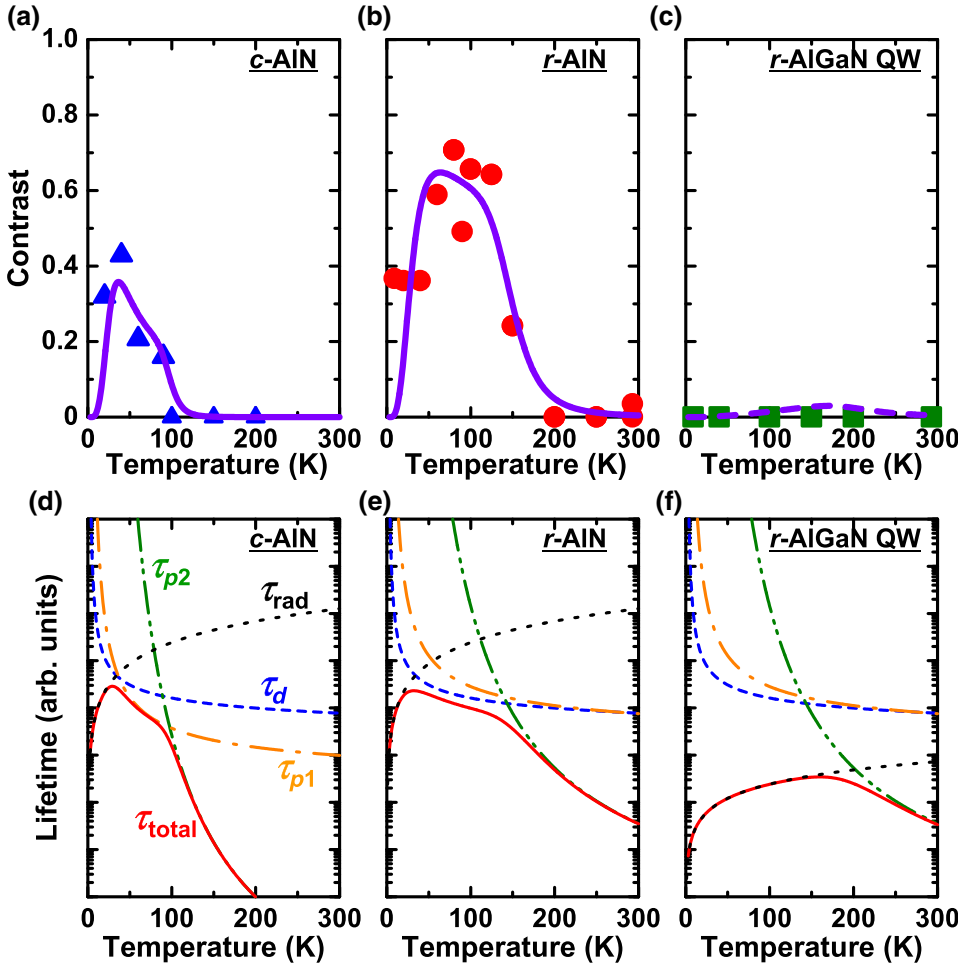


FIG. 16. Temperature dependences of the dark-spot contrasts in (a) the *c*-plane AlN film, (b) the *r*-plane AlN film, and (c) the *r*-plane Al<sub>0.8</sub>Ga<sub>0.2</sub>N/AlN QW. Solid lines in (a) and (b) show the contrasts fitted with Eq. (32). In (c), the broken line is the calculated result using the appropriate estimation of  $\tau_{\text{rad}}$ . Temperature dependences of the recombination lifetimes in the *c*-plane AlN film, the *r*-plane AlN film, and the *r*-plane Al<sub>0.8</sub>Ga<sub>0.2</sub>N/AlN QW are calculated as shown in (d), (e), and (f), respectively, which reproduce the solid and broken lines in (a), (b), and (c). In (d), (e), and (f), dotted, broken, dash-dotted, dash-double-dotted, and solid lines represent  $\tau_{\text{rad}}$ ,  $\tau_D$ ,  $\tau_{p1}$ ,  $\tau_{p2}$ , and  $\tau_{\text{total}}$ , respectively.

*r*-planes AlN films that provide the best fits in Figs. 16(a) and 16(b), respectively. Here, the total recombination lifetime in the vicinity of a TD is expressed as

$$\frac{1}{\tau_{\text{total}}} = \frac{1}{\tau_{\text{rad}}} + \frac{1}{\tau_D} + \frac{1}{\tau_{p1}} + \frac{1}{\tau_{p2}}, \quad (34)$$

where  $\tau_{p1}$  and  $\tau_{p2}$  are the nonradiative recombination lifetimes due to P1 and P2, respectively. Equation (34) indicates that the shortest lifetime dominates  $\tau_{\text{total}}$ . In other words, a recombination process with the shortest lifetime is the dominant recombination path. Therefore, the temperature variation of the dominant recombination path can be determined from Figs. 16(d) and 16(e). Table II lists the

TABLE I. Activation energies of TDs and PDs in AlN.  $E_{ad}$  is estimated from the fits of Eq. (32) to the CL contrast, as shown in Figs. 16(a) and 16(b).  $E_{ap1}$ , and  $E_{ap2}$  are estimated from the fits of Eq. (25) to the PL intensity, as shown in Fig. 11.

$E_{ad}$ (meV)	$E_{ap1}$ (meV)	$E_{ap2}$ (meV)
2.5	10	130

results. The dominant nonradiative recombination paths in the vicinity of TDs change from TDs (or P1) to P2 as the temperature increases.

On the other hand, for Al<sub>x</sub>Ga<sub>1-x</sub>N/AlN QWs, dark spots are not observed at any temperature (Fig. 5). Generally, the radiative recombination lifetimes in QWs are much shorter than those in films, and their temperature dependences differ [ $\gamma = 3/2$  for bulk and 1 for QW in Eq. (22)]. These are due to the lower dimensional confinement of excitons in QWs. Assuming that the nonradiative recombination lifetimes in QWs are the same as those in AlN films, the temperature variations of the contrasts and the recombination lifetimes are calculated as shown in Figs. 16(c) and 16(f), respectively. Figure 16(f) shows that the dominant recombination paths are changed from radiative to P2-mediated nonradiative recombinations without going through the TD-dominant region (Table II) due to the shorter QW radiative recombination lifetime. This is why dark spots are not observed at any temperature. The emission intensities of QWs are less affected by TDs than those of AlN films.

For both the AlN films and Al<sub>x</sub>Ga<sub>1-x</sub>N QWs, the dark-spot contrasts are considerably weakened at RT because

TABLE II. Dominant recombination paths in the vicinity of TDs in the whole temperature region. Rad means radiative recombination.

Sample	0–30 K	30–100 K	100–140 K	140–200 K	200 K –
<i>c</i> -AlN	Rad	(TD →) P1		P2	
<i>r</i> -AlN	Rad		TD		P2
QW			Rad		P2

P2 becomes the dominant recombination center. It is noteworthy that these contrast behaviors completely differ from those in GaN and Ga-rich  $\text{Al}_x\text{Ga}_{1-x}\text{N}$  [50–53]. Unlike AlN and Al-rich  $\text{Al}_x\text{Ga}_{1-x}\text{N}$ , dark spots due to TDs are clearly observed for GaN even at RT, implying that  $\tau_D$  is shorter than  $\tau_p$  even at RT in GaN. This may be because the density of Ga vacancies ( $V_{\text{Ga}}$ ) in GaN is much lower than that of  $V_{\text{Al}}$  in AlN. This assertion is supported by the theoretical consideration showing that the formation energy of  $V_{\text{Ga}}$  is larger than that of  $V_{\text{Al}}$  [39]. Therefore, more attention should be paid to PDs and their activities in AlN and Al-rich  $\text{Al}_x\text{Ga}_{1-x}\text{N}$  compared with GaN and Ga-rich  $\text{Al}_x\text{Ga}_{1-x}\text{N}$ . In fact, the impacts of TDs in AlN (in Fig. 6) are much smaller than those of GaN [54].

To compare the impact of nonradiative recombination centers on the emission intensity near TDs for *c*- and *r*-planes AlN films, we defined the nonradiative recombination parameter  $M_i$  as  $N_{ii}\sigma_{0i}$ . Because  $\sigma_{0i}$  is the capture cross section at  $T \rightarrow \infty$  [see Eq. (20)],  $M_i$  means a carrier density captured by the defects (corresponding to *i*) at  $T \rightarrow \infty$ . Therefore, the nonradiative recombination rate due to the defect is proportional to  $M_i$  at any temperature. Hence,  $M_i$  is an effective index to characterize the impact of a defect. Note that  $\sigma_{0i}$  is basically determined by the material and the defect type.

When the dark-spot contrasts are fitted with Eq. (32) [Figs. 16(a) and 16(b)], we obtain  $F_i$  [expressed as Eq. (33)] as the fitting parameters. Although  $\alpha$ , which is related to the radiative recombination lifetime [see Eq. (22)], is not determined by the fit, we can exclude its influence by calculating the ratio of  $F_i$  to  $F_d$  as

$$\begin{aligned} \frac{F_i}{F_d} &= \frac{N_{ii}\sigma_{0i}}{N_{id}\sigma_{0d}} \\ &= \frac{M_i}{M_d}. \end{aligned} \quad (35)$$

As previously mentioned,  $F_d$  ( $M_d$ ) should have the same value in the *c*- and *r*-planes AlN films. Therefore,  $M_i/M_d$

can be a relative index to evaluate the impact of PDs with respect to TDs.  $M_i/M_d$  in *c*- and *r*-planes AlN calculated by Eq. (35) are shown in Table III.  $M_i/M_d$  greater than unity indicates that P1 and P2 predominantly act as nonradiative recombination centers compared with TDs at sufficiently high temperatures even in the vicinity of TDs. Despite the large activation energy, P2 can be a dominant nonradiative recombination center at RT in AlN films because  $M_{p2}$  is remarkably larger than  $M_d$  and  $M_{p1}$ . Considering that  $\sigma_{0i}$  should be the same for the same type of defects in AlN films, the relative trap density of the same type defects between the *c*- and *r*-planes AlN films can be calculated as

$$\begin{aligned} \frac{M_i^{(c)}/M_d}{M_i^{(r)}/M_d} &= \frac{M_i^{(c)}}{M_i^{(r)}} \\ &= \frac{N_{ii}^{(c)}}{N_{ii}^{(r)}}, \end{aligned} \quad (36)$$

where the superscript characters (*c*) and (*r*) mean the *c*-plane and *r*-plane, respectively. The P1 and P2 densities ( $N_{p1}$  and  $N_{p2}$ ) in *c*-plane AlN estimated by Eq. (36) are 7.6 times and 540 times as large as those in *r*-plane AlN, respectively. This result well explains the shorter  $L_{\text{eff}}$  and the weaker  $C_{\text{max}}$  in *c*-plane AlN at RT in Sec. III A.

## 2. Prediction of the defect-density dependence of macroscopic efficiency degradation

Thus far, we have demonstrated that the macroscopic emission efficiency of AlN and Al-rich  $\text{Al}_x\text{Ga}_{1-x}\text{N}$  with relatively low TDDs is determined by the competition between radiative recombination and nonradiative recombination due to PDs at any temperature (Fig. 7). On the other hand, the local efficiency in the vicinity of TDs is affected by TDs or PDs, depending on the temperature (Fig. 16). Here, we predict the dominant nonradiative recombination center and the consequent macroscopic efficiency of AlN as functions of TD and PD densities.

When the PD densities vary from  $N_{p1}$  ( $N_{p2}$ ) to  $N'_{p1}$  ( $N'_{p2}$ ), the relative PD density is defined as

$$R_i = \frac{N'_{ii}}{N_{ii}}, \quad (37)$$

where  $i = p1$  or  $p2$ . The dark-spot contrast ( $C_{\text{max}}$ ) and effective diffusion length ( $L_{\text{eff}}$ ) accordingly vary. They can be rewritten using Eqs. (3), (4), (32), (33), and (37) as

$$C'_{\text{max}}(T) = \frac{1 + T^{\gamma+1/2} [F_d \exp(-E_{ad}/k_B T) + F_{p1} \exp(-E_{ap1}/k_B T) + F_{p2} \exp(-E_{ap2}/k_B T)]}{1 + T^{\gamma+1/2} [F_d \exp(-E_{ad}/k_B T) + F_{p1} R_{p1} \exp(-E_{ap1}/k_B T) + F_{p2} R_{p2} \exp(-E_{ap2}/k_B T)]} \times C_{\text{max}}(T), \quad (38)$$

and

$$L_{\text{eff}}^2(T) = \frac{D_{\text{diff}}\tau'_{\text{eff}}}{D_{\text{diff}}\tau_{\text{eff}}} \times L_{\text{eff}}^2(T) = \frac{1 + T^{\gamma+1/2} [F_{p1} \exp(-E_{ap1}/k_B T) + F_{p2} \exp(-E_{ap2}/k_B T)]}{1 + T^{\gamma+1/2} [F_{p1} R_{p1} \exp(-E_{ap1}/k_B T) + F_{p2} R_{p2} \exp(-E_{ap2}/k_B T)]} \times L_{\text{eff}}^2(T), \quad (39)$$

respectively, where  $\tau'_{\text{eff}}$  is the effective carrier recombination lifetime reflecting the changes of the defect densities. For simplicity,  $D_{\text{diff}}$  is assumed to be unaffected by the PD-density variation, similar to the discussion in Sec. 4.  $C_{\text{max}}(T)$  and  $L_{\text{eff}}(T)$  at certain temperatures are experimentally obtained, and the remaining parameters except for  $R_i$  are estimated by the aforementioned fits.

$\eta_{\text{TD}}$  in Eq. (16), which is an index of the impact of TDs on efficiency degradation, can be described as a function of  $R_i$  using  $C'_{\text{max}}(T)$  and  $L'_{\text{eff}}(T)$ , which are expressed in Eqs. (38) and (39), instead of  $C_{\text{max}}$  and  $L_{\text{eff}}$ , respectively. When TDD is fixed at  $1 \times 10^8 \text{ cm}^{-2}$ ,  $\eta_{\text{TD}}$  at 293 K is calculated as shown in Fig. 17(a), where  $N_{tp1}$  and  $N_{tp2}$  vary with respect to the trap densities in  $r$ -plane AlN [using  $N_{ti}^{(r)}$  as a denominator of  $R_i$  in Eq. (37)]. In Fig. 17(a),  $\eta_{\text{TD}} = 100\%$  means that the dominant nonradiative recombination centers are PDs. Both the  $c$ - and  $r$ -planes AlN films investigated in this study are located in the P2-dominant region. For example, to achieve  $\eta_{\text{TD}} < 50\%$  in the  $r$ -plane AlN film, Fig. 17(a) indicates that P2 should be decreased by  $< 1/65$ . On the other hand, additional P1 reduction followed by a substantial decrease in P2 ( $< 1/10^4$ ) is required for the  $c$ -plane AlN film. This is due to the large  $M_{p1}$  (Table III).

The NBE emission intensity  $I_{\text{NBE}}(T)$  defined as Eq. (19) can also be evaluated. The relative NBE emission intensity is expressed using Eqs. (3), (10), and (15) as

$$\frac{I'_{\text{NBE}}(T)}{I_{\text{NBE}}(T)} = \frac{\eta'_{\text{TD}}\tau'_{\text{eff}}}{\eta_{\text{TD}}\tau_{\text{eff}}} = \frac{\eta'_{\text{TD}}L_{\text{eff}}^2(T)}{\eta_{\text{TD}}L_{\text{eff}}^2(T)}, \quad (40)$$

where  $\eta'_{\text{TD}}$  means  $\eta_{\text{TD}}$  reflecting the variations of the defect densities and is calculated in Fig. 17(a).

Then the relative NBE emission intensity at 293 K normalized by that of  $r$ -plane AlN under the same conditions as Fig. 17(a) is calculated using Eq. (40). Figure 17(b) shows the calculation result. Reducing P1 does not improve the emission intensity of  $r$ -plane AlN, whereas reducing P2 ( $< 1/65$ ) can increase the current emission intensity by 20 times. A similar tendency also occurs for

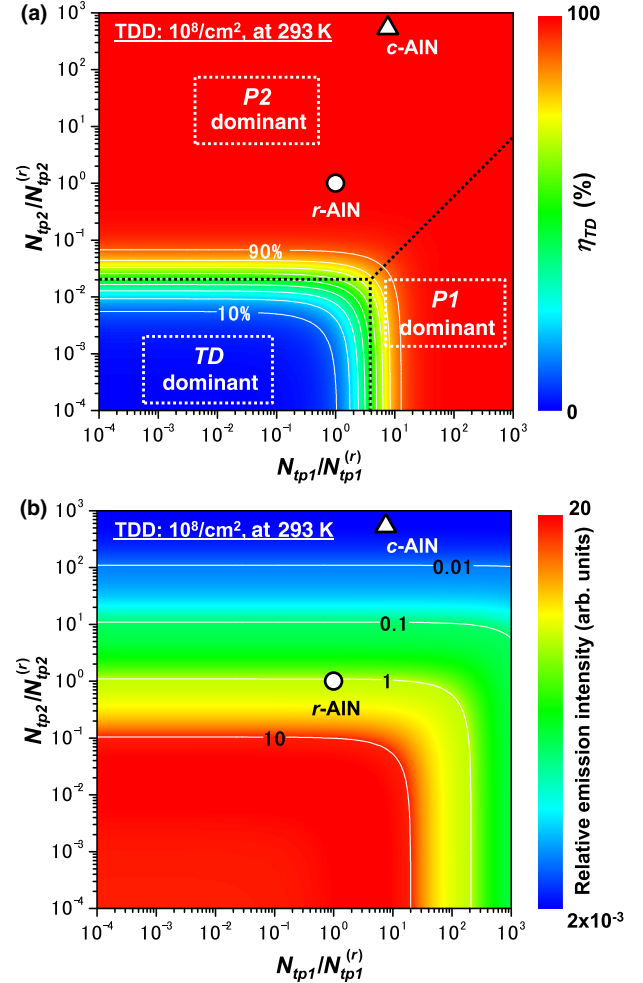


FIG. 17. (a) Calculated  $\eta_{\text{TD}}$  at 293 K when TDD is fixed at  $1 \times 10^8 \text{ cm}^{-2}$ , while  $N_{tp1}$  and  $N_{tp2}$  are varied.  $N_{tp1}$  and  $N_{tp2}$  relatively vary with respect to the trap densities in  $r$ -plane AlN. (b) Relative emission intensity is calculated under the same conditions as (a).

$c$ -plane AlN; the intensity improvement rate by reducing P2 ( $< 1/10^4$ ) should be three orders of magnitude higher than  $r$ -plane AlN. This is due to the large  $M_{p2}$  in  $c$ -plane AlN (Table III).

TABLE III. Nonradiative recombination parameters  $M_i$  ( $= N_{it}\sigma_{0i}$ ) normalized by  $M_d$ . Here,  $M_d$  is fixed in both  $c$ -AlN and  $r$ -AlN because  $N_{td}$  and  $\sigma_{0d}$  are basically determined by the material.

Sample	$M_d/M_d$	$M_{p1}/M_d$	$M_{p2}/M_d$
$c$ -AlN	1.0	10	$1.6 \times 10^7$
$r$ -AlN		1.4	$3.0 \times 10^4$

In the same way as Fig. 17(a),  $\eta_{TD}$  at 293 K is calculated with fixed  $N_{p1}$  ( $= N_{p1}^{(r)}$ ), while TDD and  $N_{p2}$  are varied. Figure 18(a) shows results, where  $N_{p2}$  is varied relative to the trap density in  $r$ -plane AlN. Furthermore, Fig. 18(b) shows the emission intensity at 293 K normalized by that of  $r$ -plane AlN under the same conditions as Fig. 18(a). Similar to reducing P1 [Fig. 17(b)], reducing

TDs does not improve the emission intensity of  $r$ -plane AlN. However, reducing P2 can remarkably strengthen the emission intensity [55]. After the P2 reduction, TDs become the dominant nonradiative recombination centers, and a decrease of TDD to  $10^6 \text{ cm}^{-2}$  can achieve about a 200-times larger emission than the current intensity. At this stage, we are approaching the P1-dominant region [Fig. 18(a)]. Consequently, P1 reduction is necessary for further improvements.

#### IV. CONCLUSIONS

We performed CL and PL measurements to clarify the dominant nonradiative recombination paths in AlN and Al-rich  $\text{Al}_x\text{Ga}_{1-x}\text{N}$  structures. TDs and two types of PDs (P1 and P2) mainly act as nonradiative recombination centers, and their estimated activation energies are approximately 2.5, 10, and 130 meV, respectively. Despite the large activation energy, P2 predominantly affects the emission intensity at RT due to its high trap density. Therefore, P2 (not TDs) has to be reduced to improve the IQE of AlN and Al-rich  $\text{Al}_x\text{Ga}_{1-x}\text{N}$  structures. Since the deep-level emissions at 3.2 and 3.5–3.7 eV are enhanced by hole transfers to P2 near RT, P2 may be fully negative-charged  $V_{\text{Al}}\text{-O}_{\text{N}}$  complex defects. The formation energy of  $V_{\text{Al}}$  in AlN is smaller than that of  $V_{\text{Ga}}$  in GaN, and P2 can be easily generated in AlN and Al-rich  $\text{Al}_x\text{Ga}_{1-x}\text{N}$  structures. Hence, the impacts of TDs in AlN are much smaller than those of GaN. Because the growth conditions may change the P2 density, optimization of the growth conditions with an emphasis on the PD reduction is very important.

#### ACKNOWLEDGMENTS

We would like to acknowledge JFE Mineral Company, Ltd. for providing the AlN substrates. We also would like to thank Professor Hiramatsu and Professor Miyake (Mie University) for their support with the low-temperature CL measurements. This work is partially supported by JSPS KAKENHI Grant Nos. JP15H05732, JP16H02332, and JP16H06426.

#### APPENDIX: EVALUATION OF THE FITTING METHODS OF CL CONTRASTS

Throughout the paper, the impact of TDs on the efficiency degradation is analyzed based on the experimental CL results, where the CL contrasts are fitted with Eq. (1). Equation (1) using an exponential function is an approximation, and K. K. Sabelfeld *et al.* have recently derived a stricter expression for CL contrasts in the vicinity of TDs, which is written as [22]

$$I^B(r) = I_0 \left[ 1 - \frac{IK_0(r/L_{\text{eff}})}{L_{\text{eff}}K_1(r_0/L_{\text{eff}}) + IK_0(r_0/L_{\text{eff}})} \right]. \quad (\text{A1})$$

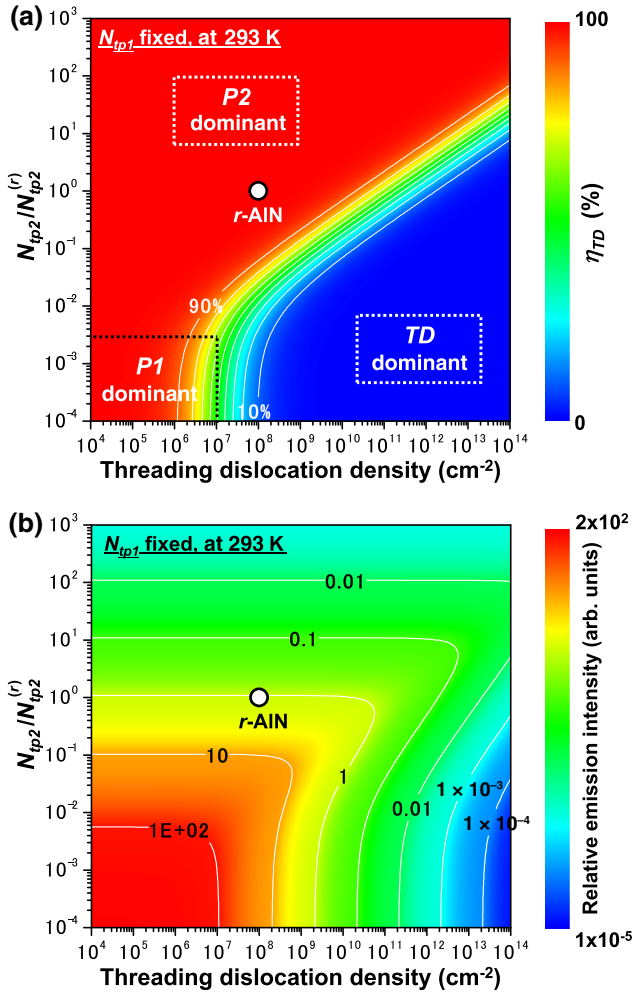


FIG. 18. (a) Calculated  $\eta_{TD}$  at 293 K when  $N_{p1}$  is fixed, while TDD and  $N_{p2}$  are varied.  $N_{p2}$  relatively varies with respect to the trap density in  $r$ -plane AlN. (b) Relative emission intensity is calculated under the same conditions as (a).



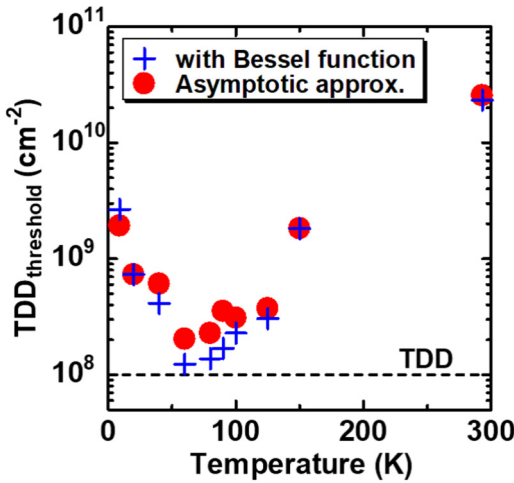


FIG. 19.  $TDD_{\text{threshold}}$  for an  $r$ -plane AlN film derived from Eqs. (1) and (A1).

Here,  $l$  is the recombination length at a dislocation,  $K_0(x)$  is the zero-order modified Bessel function of the second kind,  $K_1(x)$  is the first modified Bessel function of the second kind, and  $r_0$  is the radius of a TD. Equation (1) corresponds to the asymptotic approximation of Eq. (A1). Similar to Eq. (16) in Sec. IIIA4,  $\eta_{\text{TD}}$ , which is defined as the efficiency with respect to the efficiency in the absence of TDs, is rewritten as

$$\eta_{\text{TD}} = 1 - \int_0^\infty \int_0^{2\pi} T_D \left[ \frac{r l K_0(r/L)}{L K_1(r_0/L) + l K_0(r_0/L)} \right] d\theta dr. \quad (\text{A2})$$

The second term in Eq. (A2) is a more precise expression of the efficiency degradation due to TDs than  $2\pi L^2 C_{\text{max}} T_D$  in Eq. (16). Thus,  $TDD_{\text{threshold}}$ , which is the lowest limit of TDD that degrades the emission efficiency, is expected to be more accurately estimated from Eq. (2).

However, fits with Eq. (A1) are difficult compared with those with Eq. (1) due to the larger number of the fitting parameters. Particularly, because both  $r_0$  and  $l$  affect the recombination velocity around a TD, separately determining them from experiments is difficult. K. K. Sabelfeld *et al.* have suggested to treat  $r_0$  as a constant (1 nm) [22], but, in general,  $r_0$  depends on the condition around a TD. Moreover,  $l$  is a function of  $L_{\text{eff}}$  in our model, which makes the fitting procedure more complicated.

Thus, it is difficult to uniquely determine the parameters in Eq. (A1) for our results, and different parameter sets can equally well reproduce the CL contrast. However, it is noteworthy that once the CL contrast is reproduced, different parameter sets offer similar  $\eta_{\text{TD}}$  and  $TDD_{\text{threshold}}$  values, thereby justifying the analyses based on Eq. (A2).

To quantitatively evaluate the validity of the approximation shown in Eq. (1), Fig. 19 compares  $TDD_{\text{threshold}}$  for an  $r$ -plane AlN film derived from Eqs. (1) and (A1).

(For the fit with Eq. (A1), we assume  $r_0 = 1$  nm, as suggested in Ref. [22].) The estimated  $TDD_{\text{threshold}}$  values are almost unchanged regardless of the fitting methods. Therefore, we conclude that the asymptotic approximation expressed by Eq. (1) is effective to evaluate the TD impact on the efficiency degradation, as described in the main text. Furthermore, Eq. (1) is a good approximation in terms of uniqueness of fits, though the diffusion length is underestimated.

- 
- [1] Y. Narukawa, M. Ichikawa, D. Sanga, M. Sano, and T. Mukai, White light emitting diodes with super-high luminous efficacy, *J. Phys. D: Appl. Phys.* **43**, 354002 (2010).
  - [2] A. Khan, K. Balakrishnan, and T. Katona, Ultraviolet light-emitting diodes based on group three nitrides, *Nat. Photon.* **2**, 77 (2008).
  - [3] H. Hirayama, S. Fujikawa, N. Noguchi, J. Norimatsu, T. Takano, K. Tsubaki, and N. Kamata, 222–282 nm AlGaIn and InAlGaIn-based deep-UV LEDs fabricated on high-quality AlN on sapphire, *Phys. Stat. Solidi (a)* **206**, 1176 (2009).
  - [4] C. Pernot, M. Kim, S. Fukahori, T. Inazu, T. Fujita, Y. Nagasawa, A. Hirano, M. Ippommatsu, M. Iwaya, S. Kamiyama, I. Akasaki, and H. Amano, Improved efficiency of 255–280 nm AlGaIn-based light-emitting diodes, *Appl. Phys. Express* **3**, 061004 (2010).
  - [5] T. Kinoshita, T. Obata, T. Nagashima, H. Yanagi, B. Moody, S. Mita, S. Inoue, Y. Kumagai, A. Koukitu, and Z. Sitar, Performance and reliability of deep-ultraviolet light-emitting diodes fabricated on AlN substrates prepared by hydride vapor phase epitaxy, *Appl. Phys. Express* **6**, 092103 (2013).
  - [6] M. Shatalov, W. Sun, A. Lunev, X. Hu, A. Dobrinsky, Y. Bilenko, J. Yang, M. Shur, R. Gaska, C. Moe, G. Garrett, and M. Wraback, AlGaIn deep-ultraviolet light-emitting diodes with external quantum efficiency above 10%, *Appl. Phys. Express* **5**, 082101 (2012).
  - [7] T. Takano, T. Mino, J. Sakai, N. Noguchi, K. Tsubaki, and H. Hirayama, Deep-ultraviolet light-emitting diodes with external quantum efficiency higher than 20% at 275 nm achieved by improving light-extraction efficiency, *Appl. Phys. Express* **10**, 031002 (2017).
  - [8] R. G. Banal, M. Funato, and Y. Kawakami, Optical anisotropy in [0001]-oriented  $\text{Al}_x\text{Ga}_{1-x}\text{N}/\text{AlN}$  quantum wells ( $x > 0.69$ ), *Phys. Rev. B* **79**, 121308(R) (2009).
  - [9] Y. Iwata, R. G. Banal, S. Ichikawa, M. Funato, and Y. Kawakami, Emission mechanisms in Al-rich AlGaIn/AlN quantum wells assessed by excitation power dependent photoluminescence spectroscopy, *J. Appl. Phys.* **117**, 075701 (2015).
  - [10] R. G. Banal, M. Funato, and Y. Kawakami, Extremely high internal quantum efficiencies from AlGaIn/AlN quantum wells emitting in the deep ultraviolet spectral region, *Appl. Phys. Lett.* **99**, 011902 (2011).
  - [11] A. Bhattacharyya, T. D. Moustakas, L. Zhou, D. J. Smith, and W. Hug, Deep ultraviolet emitting AlGaIn quantum wells with high internal quantum efficiency, *Appl. Phys. Lett.* **94**, 181907 (2009).

- [12] M. Imura, K. Nakano, G. Narita, N. Fujimoto, N. Okada, K. Balakrishnan, M. Iwaya, S. Kamiyama, H. Amano, I. Akasaki, T. Noro, T. Takagi, and A. Bandoh, Epitaxial lateral overgrowth of AlN on trench-patterned AlN layers, *J. Cryst. Growth* **298**, 257 (2007).
- [13] H. Hirayama, S. Fujikawa, J. Norimatsu, T. Takano, K. Tsubaki, and N. Kamata, Fabrication of a low threading dislocation density ELO-AlN template for application to deep-UV LEDs, *Phys. Stat. Solidi (c)* **6**, S356 (2009).
- [14] K. Fujita, K. Okuura, H. Miyake, K. Hiramatsu, and H. Hirayama, HVPE growth of thick AlN on trench-patterned substrate, *Phys. Stat. Solidi (c)* **8**, 1483 (2011).
- [15] U. Zeimer, V. Kueller, A. Knauer, A. Mogilatenko, M. Weyers, and M. Kneissl, High quality AlGaIn grown on ELO AlN/sapphire templates, *J. Cryst. Growth* **377**, 32 (2013).
- [16] R. Dalmau, B. Moody, R. Schlessler, S. Mita, J. Xie, M. Feneberg, B. Neuschl, K. Thonke, R. Collazo, A. Rice, J. Tweedie, and Z. Sitar, Growth and characterization of AlN and AlGaIn epitaxial films on AlN single crystal substrates, *J. Electrochem. Soc.* **158**, H530 (2011).
- [17] S. Ichikawa, Y. Iwata, M. Funato, S. Nagata, and Y. Kawakami, High quality semipolar (1102) AlGaIn/AlN quantum wells with remarkably enhanced optical transition probabilities, *Appl. Phys. Lett.* **104**, 252102 (2014).
- [18] S. F. Chichibu, H. Miyake, Y. Ishikawa, M. Tashiro, T. Ohtomo, K. Furusawa, K. Hazu, K. Hiramatsu, and A. Uedono, Impacts of Si-doping and resultant cation vacancy formation on the luminescence dynamics for the near-band-edge emission of Al<sub>0.6</sub>Ga<sub>0.4</sub>N films grown on AlN templates by metalorganic vapor phase epitaxy, *J. Appl. Phys.* **113**, 213506 (2013).
- [19] S. F. Chichibu, K. Hazu, Y. Ishikawa, M. Tashiro, T. Ohtomo, K. Furusawa, A. Uedono, S. Mita, J. Xie, R. Collazo, and Z. Sitar, Excitonic emission dynamics in homoepitaxial AlN films studied using polarized and spatio-time-resolved cathodoluminescence measurements, *Appl. Phys. Lett.* **103**, 142103 (2013).
- [20] See Supplemental Material at <http://link.aps.org/supplemental/10.1103/PhysRevApplied.10.064027> for a list of the used variables and the relationship between  $L$  and  $L_{\text{eff}}$ .
- [21] E. E. Yakimov, What is the real value of diffusion length in GaN? *J. Alloy Compd.* **627**, 344 (2015).
- [22] K. K. Sabelfeld, V. M. Kaganer, C. Pfüller, and O. Brandt, Dislocation contrast in cathodoluminescence and electron-beam induced current maps on GaN(0001), *J. Phys. D: Appl. Phys.* **50**, 405101 (2017).
- [23] M. Funato, K. Matsuda, R. G. Banal, R. Ishii, and Y. Kawakami, Homoepitaxy and Photoluminescence Properties of (0001) AlN, *Appl. Phys. Express* **5**, 082001 (2012).
- [24] R. Ishii, M. Funato, and Y. Kawakami, Huge electron-hole exchange interaction in aluminum nitride, *Phys. Rev. B* **87**, 161204(R) (2013).
- [25] T. Miyajima, T. Hino, S. Tomiya, K. Yanashima, H. Nakajima, Y. Nanishi, A. Satake, Y. Masumoto, K. Akimoto, T. Kobayashi, and M. Ikeda, Threading dislocations and Optical properties of GaN and GaInN, *Phys. Status Solidi B* **228**, 395 (2001).
- [26] D. Chens, S. J. Henly, and F. A. Ponce, Edge and screw dislocations as nonradiative centers in InGaIn/GaN quantum well luminescence, *Appl. Phys. Lett.* **78**, 2691 (2001).
- [27] S. Sonderegger, E. Feltin, M. Merano, A. Crottini, J. F. Carlin, R. Sachot, B. Deveaud, N. Grandjean, and J. D. Ganière, High spatial resolution picosecond cathodoluminescence of InGaIn quantum wells, *Appl. Phys. Lett.* **89**, 232109 (2006).
- [28] M. Matsubara, J. Godet, L. Pizzagalli, and E. Bellotti, Properties of threading screw dislocation core in wurtzite GaN studied by Heyd-Scuseria-Ernzerhof hybrid functional, *Appl. Phys. Lett.* **103**, 262107 (2013).
- [29] Y. Taniyasu, M. Kasu, and T. Makimoto, An aluminium nitride light-emitting diode with a wavelength of 210 nanometres, *Nature (London)* **441**, 325 (2006).
- [30] E. Bellotti and F. Bertazzi, *Nitride Semiconductor Devices*, edited by J. Piprek (WILEY-VCH, 2007) Chap. 4.
- [31] R. G. Banal, Y. Akashi, K. Matsuda, Y. Hayashi, M. Funato, and Y. Kawakami, Crack-free thick AlN films obtained by NH<sub>3</sub> nitridation of sapphire substrate, *Jpn. J. Appl. Phys.* **52**, 08JB21 (2013).
- [32] H. Miyake, G. Nishio, S. Suzuki, K. Hiramatsu, H. Fukuyama, J. Kaur, and N. Kuwano, Annealing of an AlN buffer layer in N<sub>2</sub>-CO for growth of a high-quality AlN film on sapphire, *Appl. Phys. Express* **9**, 025501 (2016).
- [33] K. Kumakura, T. Makimoto, N. Kobayashi, T. Hashizume, T. Fukui, and H. Hasegawa, Minority carrier diffusion length in GaN: Dislocation density and doping concentration dependence, *Appl. Phys. Lett.* **86**, 052105 (2005).
- [34] S. Hafiz, F. Zhang, M. Monavarian, V. Avrutin, H. Morkoç, U. Özgür, S. Metzner, F. Bertram, J. Christen, and B. Gil, Determination of carrier diffusion length in GaN, *J. Appl. Phys.* **117**, 013106 (2015).
- [35] T. Malin, A. Gilinsky, V. Mansurov, D. Protasov, E. Yakimov, and K. Zhuravlev, Minority carrier diffusion length in Al<sub>x</sub>Ga<sub>1-x</sub>N ( $x = 0.1$ ) grown by ammonia molecular beam epitaxy, *Phys. Stat. Solidi (c)* **12**, 447 (2015).
- [36] M. Kneissl, T. Kolbe, C. Chua, V. Kueller, N. Lobo, J. Stellmach, A. Knauer, H. Rodriguez, S. Einfeldt, Z. Yang, N. M. Johnson, and M. Weyers, Advances in group III-nitride-based deep UV light-emitting diode technology, *Semicond. Sci. Technol.* **26**, 014036 (2011).
- [37] G.-D. Hao, N. Tamari, T. Obata, T. Kinoshita, and S. Inoue, Electrical determination of current injection and internal quantum efficiencies in AlGaIn-based deep-ultraviolet light-emitting diodes, *Opt. Express* **25**, A639 (2017).
- [38] D. Cherns and M. E. Hawkrige, The structure and properties of dislocations in GaN, *J. Mater. Sci.* **41**, 2685 (2006).
- [39] K. Laaksonen, M. G. Ganchenkova, and R. M. Nieminen, Vacancies in wurtzite GaN and AlN, *J. Phys.: Condens. Matter* **21**, 015803 (2009).
- [40] D. V. Lang and C. H. Henry, Nonradiative Recombination at Deep Levels in GaAs and GaP by Lattice-Relaxation Multiphonon Emission, *Phys. Rev. Lett.* **35**, 1525 (1975).
- [41] J. Feldmann, G. Peter, E. O. Göbel, P. Dawson, K. Moore, C. Foxon, and R. J. Elliott, Linewidth Dependence of Radiative Exciton Lifetimes in Quantum Wells, *Phys. Rev. Lett.* **59**, 2337 (1987).
- [42] H. Akiyama, S. Koshihara, T. Someya, K. Wada, H. Noge, Y. Nakamura, T. Inoshita, A. Shimizu, and H. Sakaki, Thermalization Effect on Radiative Decay of Excitons in Quantum Wires, *Phys. Rev. Lett.* **72**, 924 (1994).

- [43] R. Ishii, M. Funato, and Y. Kawakami, Effects of strong electron-hole exchange and exciton-phonon interactions on the exciton binding energy of aluminum nitride, *Jpn. J. Appl. Phys.* **53**, 091001 (2014).
- [44] X. Tang, F. Hossain, K. Wongchotigul, and M. G. Spencer, Near band-edge transition in aluminum nitride thin films grown by metal organic chemical vapor deposition, *Appl. Phys. Lett.* **72**, 1501 (1998).
- [45] A. Sedhain, L. Du, J. H. Edgar, J. Y. Lin, and H. X. Jiang, The origin of 2.78 eV emission and yellow coloration in bulk AlN substrates, *Appl. Phys. Lett.* **95**, 262104 (2009).
- [46] A. Sedhain, J. Y. Lin, and H. X. Jiang, Nature of optical transitions involving cation vacancies and complexes in AlN and AlGaIn, *Appl. Phys. Lett.* **100**, 221107 (2012).
- [47] T. Koyama, M. Sugawara, T. Hoshi, A. Uedono, J. F. Kaeding, R. Sharma, S. Nakamura, and S. F. Chichibu, Relation between Al vacancies and deep emission bands in AlN epitaxial films grown by NH<sub>3</sub>-source molecular beam epitaxy, *Appl. Phys. Lett.* **90**, 241914 (2007).
- [48] C. Stampfl and C. G. Van de Walle, Theoretical investigation of native defects, impurities, and complexes in aluminum nitride, *Phys. Rev. B* **65**, 155212 (2002).
- [49] Q. Yan, A. Janotti, M. Scheffler, and C. G. Van de Walle, Origins of optical absorption and emission lines in AlN, *Appl. Phys. Lett.* **105**, 111104 (2014).
- [50] M. Albrecht, J. L. Weyher, B. Lucznik, I. Grzegory, and S. Porowski, Nonradiative recombination at threading dislocations in *n*-type GaN: Studied by cathodoluminescence and defect selective etching, *Appl. Phys. Lett.* **92**, 231909 (2008).
- [51] G. Naresh-Kumar, J. Bruckbauer, P. R. Edwards, S. Krausel, B. Hourahine, R. W. Martin, M. J. Kappers, M. A. Moram, S. Lovelock, R. A. Oliver, C. J. Humphreys, and C. Trager-Cowan, Coincident electron channeling and cathodoluminescence studies of threading dislocations in GaN, *Microsc. Microanal.* **20**, 55 (2014).
- [52] J. Liang, X. Hongling, W. Xiaoliang, W. Cuimei, D. Qingwen, L. Zhidong, D. Jieqin, W. Zhanguo, and H. Xun, The growth and characterization of GaN films on cone-shaped patterned sapphire by MOCVD, *J. Semicond.* **34**, 113002 (2013).
- [53] S. Kamiyama, M. Iwaya, H. Amano, and I. Akasaki, Heteroepitaxial technology for high-efficiency UV light-emitting diode, *Opto-Electronics Rev.* **10**, 225 (2002).
- [54] S. Y. Karpov and Y. N. Makarov, Dislocation effect on light emission efficiency in gallium nitride, *Appl. Phys. Lett.* **81**, 4721 (2002).
- [55] When TDD is too high (for example,  $> 10^{13} \text{ cm}^{-2}$ ), P2 reduction may decrease the emission intensity because the excited carriers are more easily captured by TDs due to the elongated diffusion length.